

AD-A252 969



2

NAVAL POSTGRADUATE SCHOOL
Monterey, California



DTIC
ELECTE
JUL 20 1992
S B D

THESIS

PREPARATION OF EXTINCTION FREE
 γ Ti-51at.%Al ALLOY POWDER AND
CHARACTERIZATION BY X-RAY DIFFRACTION

by

Troy A. Stoner

March, 1992

Thesis Advisor:

Alan G. Fox

Approved for public release; distribution is unlimited.

92 7 17 043

92-19035



Unclassified

SECURITY CLASSIFICATION OF THIS PAGE

REPORT DOCUMENTATION PAGE				Form Approved OMB No 0704-0188	
1a REPORT SECURITY CLASSIFICATION UNCLASSIFIED			1b RESTRICTIVE MARKINGS		
2a SECURITY CLASSIFICATION AUTHORITY		3 DISTRIBUTION / AVAILABILITY OF REPORT			
2b DECLASSIFICATION / DOWNGRADING SCHEDULE					
4 PERFORMING ORGANIZATION REPORT NUMBER(S)			5 MONITORING ORGANIZATION REPORT NUMBER(S)		
6a NAME OF PERFORMING ORGANIZATION Naval Postgraduate School		6b OFFICE SYMBOL (If applicable) ME	7a. NAME OF MONITORING ORGANIZATION Naval Postgraduate School		
6c. ADDRESS (City, State, and ZIP Code) Monterey, CA 93943-5000			7b ADDRESS (City, State, and ZIP Code) Monterey, CA 93943-5000		
8a NAME OF FUNDING / SPONSORING ORGANIZATION Naval Air Development Center		8b OFFICE SYMBOL (If applicable) Code 6063	9 PROCUREMENT INSTRUMENT IDENTIFICATION NUMBER		
8c. ADDRESS (City, State, and ZIP Code) Warminster, PA 18974			10 SOURCE OF FUNDING NUMBERS		
			PROGRAM ELEMENT NO	PROJECT NO	TASK NO
			WORK UNIT ACCESSION NO		
11 TITLE (Include Security Classification) PREPARATION OF EXTINCTION FREE GAMMA Ti-51at.ZAl ALLOY POWDER AND CHARACTERIZATION BY X-RAY DIFFRACTION (UNCLASSIFIED)					
12 PERSONAL AUTHOR(S) Stoner, Troy A.					
13a TYPE OF REPORT Master's Thesis		13b TIME COVERED FROM _____ TO _____	14 DATE OF REPORT (Year, Month, Day) 1992, March		15 PAGE COUNT 78
16 SUPPLEMENTARY NOTATION The views expressed in this thesis are those of the author and do not reflect the policy or position of the Department of Defense or the United States Government.					
17 COSATI CODES			18 SUBJECT TERMS (Continue on reverse if necessary and identify by block number)		
FIELD	GROUP	SUB-GROUP	X-ray Diffraction, XRD, TiAl, titanium, aluminum, bonding characteristics, titanium aluminides, Debye-Waller temperature factor, structure factor, lattice parameter		
19 ABSTRACT (Continue on reverse if necessary and identify by block number) The lattice parameters, structure factors, and Debye-Waller temperature factor of a homogenized, binary Ti-51at.ZAl intermetallic alloy were determined using powder X-ray diffraction (XRD). Previous studies have been hampered by extinction at low Bragg angles, therefore improved powdering methods were implemented. The powder was produced by pulverizing lathe turnings taken from the sample ingot using a ceramic mortar and pestle. Then the powder was passed through a U.S. Standard #400 sieve mesh (38 microns). After further grinding a new acoustical sieving procedure was performed where powder particles were passed through a 2000 line per inch sieve mesh (5-7 microns). Next the powder was annealed to relieve induced stress produced during grinding. An X-ray diffraction study was conducted for Bragg angles 10-140°. The Li. structured TiAl lattice parameters of a₀=4.002Å and c₀=4.081Å were determined using XRD peak positions. The resulting c/a ratio equalled 1.02. The measured integrated intensities of the Fundamental reflections were used to determine a Debye-Waller temperature factor of					
20 DISTRIBUTION / AVAILABILITY OF ABSTRACT <input checked="" type="checkbox"/> UNCLASSIFIED/UNLIMITED <input type="checkbox"/> SAME AS RPT <input type="checkbox"/> DTIC USERS			21 ABSTRACT SECURITY CLASSIFICATION Unclassified		
22a NAME OF RESPONSIBLE INDIVIDUAL Alan G. Fox			22b TELEPHONE (Include Area Code) (408) 646-2142		22c OFFICE SYMBOL ME/Fx

DD Form 1473, JUN 86

Previous editions are obsolete.

S/N 0102-LF-014-6603

SECURITY CLASSIFICATION OF THIS PAGE

Unclassified

(Block 19 continued)

$B=0.65\text{\AA}^2$ using the Wilson Method. These values were determined to be accurate based on comparison to previous research and theoretical approximations. The effects of extinction at low angles were not completely avoided with the refined powder particle size however, they were significantly reduced.

Accession For	
NTIS GRA&I	<input checked="" type="checkbox"/>
DTIC TAB	<input type="checkbox"/>
Unannounced	<input type="checkbox"/>
Justification	
By _____	
Distribution/	
Availability Codes	
Dist	Avail and/or Special
A-1	

DTIC QUALITY INSPECTED 2

Approved for public release; distribution is unlimited.

Preparation of Extinction Free γ Ti - 51at.%Al Alloy Powder and
Characterization by X-Ray Diffraction

by

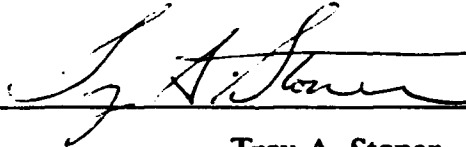
Troy A. Stoner
Lieutenant, United States Navy
B.S., United States Naval Academy, 1985

Submitted in partial fulfillment
of the requirements for the degree of

MASTER OF SCIENCE IN MECHANICAL ENGINEERING
from the
NAVAL POSTGRADUATE SCHOOL

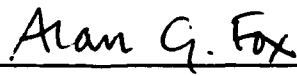
March 1992

Author:



Troy A. Stoner

Approved by:



Alan G. Fox, Thesis Advisor



Anthony J. Healey, Chairman,
Department of Mechanical Engineering

ABSTRACT

The lattice parameters, structure factors, and Debye-Waller temperature factor of a homogenized, binary Ti-51at.%Al intermetallic alloy were determined using powder X-ray diffraction (XRD). Previous studies have been hampered by extinction at low Bragg angles, therefore improved powdering methods were implemented. The powder was produced by pulverizing lathe turnings taken from the sample ingot using a ceramic mortar and pestle. Then the powder was passed through a U.S. Standard #400 sieve mesh (38 μ m). After further grinding a new acoustical sieving procedure was performed where powder particles were passed through a 2000 line per inch sieve mesh (5-7 μ m). Next the powder was annealed to relieve the induced stress produced during grinding. An X-ray diffraction study was conducted for Bragg angles 10-140°. The L1₀ structured TiAl lattice parameters of $a_0 = 4.002\text{\AA}$ and $c_0 = 4.081\text{\AA}$ were determined using XRD peak positions. The resulting c/a ratio equalled 1.02. The measured integrated intensities of the Fundamental reflections were used to determine a Debye-Waller temperature factor of $B = 0.65\text{\AA}^2$ using the Wilson Method. These values were determined to be accurate based on comparison to previous research and theoretical approximations. The effects of extinction at low Bragg angles were not completely avoided with the refined powder particle size; they were, however, significantly reduced.

TABLE OF CONTENTS

I. INTRODUCTION	1
II. BACKGROUND	3
A. TITANIUM ALUMINUM ALLOYS	3
1. Development History	3
2. Current Research Emphasis	5
B. MATERIAL CHARACTERISTICS	6
1. Microstructure	6
a. Characteristics of the TiAl Phase Diagram	6
b. Crystallography	8
2. Strength and Ductility	11
a. Deformation Mechanisms	11
b. Effects of Alloying	14
3. Methods of Analysis	15
a. X-ray Pendellösung Measurement	17
b. γ -ray Diffraction	18
c. Electron Diffraction	18

d.	X-ray Diffraction	18
C.	FUNDAMENTALS OF X-RAY DIFFRACTION	19
1.	Bragg's Law	19
2.	Diffraction Intensity Calculations	21
a.	Structure Factor	22
b.	Atomic Scattering Factor	24
c.	Multiplicity Factor	25
d.	Lorentz-Polarization Factor	25
e.	Temperature Factor	25
3.	Lattice Parameter Calculations	30
4.	Debye-Waller Temperature Factor	31
5.	Causes of Diffraction Peak Error	32
a.	Peak Position Error	32
b.	Peak Broadening Effects	32
c.	Intensity Error	33
(1)	Preferred Orientation.	33
(2)	Absorption and Extinction.	33
(3)	Intensity Scatter.	35
D.	SCOPE OF PRESENT WORK	37

III. EXPERIMENTAL PROCEDURE	38
A. ALLOY COMPOSITION AND HEAT TREATMENT	38
B. POWDER PREPARATION	38
1. Powdering	38
2. Sieving	39
3. Annealing	39
4. Powder Particle Size Measurement	40
C. X-RAY DIFFRACTION	42
IV. RESULTS AND DISCUSSION	43
A. SAMPLE ANALYSIS	43
1. Previous Research	43
2. Powder Particle Size	43
B. X-RAY DIFFRACTION RESULTS	45
1. Lattice Parameters	47
2. Debye-Waller Factor	50
V. CONCLUSIONS	54
VI. RECOMMENDATIONS	56

V. CONCLUSIONS	54
VI. RECOMMENDATIONS	56
APPENDIX A. XRD REFLECTIONS AND INTEGRATED INTENSITIES	57
APPENDIX B. NELSON-RILEY EXTRAPOLATION DATA	59
APPENDIX C. WILSON PLOT DATA	60
LIST OF REFERENCES	62
INITIAL DISTRIBUTION LIST	66

LIST OF TABLES

TABLE I.	PROPERTIES OF HIGH TEMPERATURE ALLOYS	4
TABLE II.	INTENSITY MEASUREMENTS ON DIFFERENT SIZE FRACTIONS OF <325 - MESH QUARTZ POWDERR ...	35
TABLE III.	REFLECTIONS POSITIONS AND INTEGRATED INTENSITIES	57
TABLE IV.	NELSON-RILEY EXTRAPOLATION DATA (a)	59
TABLE V.	NELSON-RILEY EXTRAPOLATION DATA (c)	59
TABLE VI.	WILSON PLOT DATA: FUNDAMENTAL REFLECTIONS	60
TABLE VII.	WILSON PLOT DATA: SUPERLATTICE REFLECTIONS	61

LIST OF FIGURES

Figure 1. Ti-Al Phase Diagram	7
Figure 2. Proposed Revisions to Ti-Al Phase Diagram	9
Figure 3. L1 ₀ Face Centered Tetragonal TiAl Lattice Structure	10
Figure 4. Tensile Test Data	12
Figure 5. Possible Burger's Vectors of T.Al	13
Figure 6. Charge Density Contour of L1 ₀ TiAl (100) Plane	16
Figure 7. Bragg's Law Geometry	20
Figure 8. Intensity Peak with K $\alpha_1\alpha_2$ Doublet	22
Figure 9. Effect of Thermal Vibration.	27
Figure 10. Ti Ellipsoid of Thermal Vibration	29
Figure 11. Intensity Deviations Associated with Crystallite Size	36
Figure 12. Sieve Assembly	40
Figure 13. Acoustic Sieve	41
Figure 14. SEM Micrograph of Powder Particle Size at 2000X	44
Figure 15. Specimen Tested Profile of (111) Diffraction Peak	46
Figure 16. McCullough et al. High Temperature XRD TiAl Profiles	46

Figure 17. Nelson-Riley Extrapolation for Lattice Parameter a_0	47
Figure 18. Nelson-Riley Extrapolation for Lattice Parameter c_0	48
Figure 19. Lattice Parameter Comparison	49
Figure 20. Debye-Waller Factor Determination from Fundamental Reflections	51
Figure 21. Extinction Effects Comparison from Fundamental Reflections	52
Figure 22. Debye-Waller Determination from Superlattice Reflections	53

ACKNOWLEDGEMENTS

I wish to express my sincere appreciation to my thesis advisor, Dr. Alan G. Fox, for his guidance and morale support during the course of this research effort. I would also like to thank LT Steven C. Cade, USN for his earlier research.

Special thanks is extended to Jenifer Hogan and my family for their patience and understanding throughout the course of my graduate studies.

I. INTRODUCTION

In recent years, γ TiAl alloys have been under extensive investigation for use in the aerospace industry due to their high specific strength at elevated temperatures while being of relatively low density. These ordered intermetallic alloys have a L1₀ type structure which remains ordered up to their melting point (1450°C); this gives them a distinctive advantage over conventional titanium alloys (<10 at.% Al) commonly used in low and medium temperature regions of jet engines. However, the limited ductilities of the tetragonal structured γ TiAl alloys at low temperatures prevent cost effective fabrication. [Ref. 1: p. 37]

Most of the research over the past 10 to 15 years has been concentrated on overcoming the alloys inherent brittleness with the addition of β -stabilizing elements such as molybdenum, niobium, gallium, vanadium, and ruthenium in an attempt to refine the microstructure and reduce the slip length. Ternary alloying has produced successful applications up to 600°C, as well as, extensive information concerning the resulting microstructural changes and dislocation behavior. However, attempts to exploit the γ TiAl alloys' full potential of 900°C have been unsuccessful to date. [Ref. 2: p. 106]

The key to a solution for the low temperature brittleness problem may lie in a better understanding of the interatomic bonding of the L1₀ structured γ TiAl. Prior to a comprehensive electron charge density study of titanium aluminides' interatomic bonding mechanisms, accurate structure factor measurements are required.

As a follow on to Fox and Cade's investigation [Ref. 3] of lattice structure and Debye-Waller temperature factor, this study will utilize X-ray diffraction on an ostensibly extinction free γ Ti-51at%Al alloy powder. A new acoustic sieving process will be performed to produce sub 5 μ m particle size powder to improve the accuracy of the diffracted intensity measurements at low angles. This will accomplish two goals: one, comparison and analysis of the improvements associated with refined particle size on extinction and two, the verification of previously measured Debye-Waller temperature factors for use in the determination of electron charge distributions necessary for the characterization of the γ TiAl bonding mechanisms.

II. BACKGROUND

A. TITANIUM ALUMINUM ALLOYS

1. Development History

In the past fifty years chemical, petroleum, medical and marine technologies have greatly benefitted from the superb qualities of high specific strength and resistance to corrosion and oxidation produced by alloying titanium. Ductile pure titanium hardens significantly with addition of alloys producing strengths of over 1000Mpa while remaining of relatively low density. These attributes combined with high melting points and resistance to creep have made titanium alloys the preferred material for applications in the aerospace industry, in particular titanium aluminides. The most commonly used titanium alloy in the aerospace industry is Ti-6Al-4V (weight percent). First produced in the 1950's, it is known as IMI318 in the United Kingdom and is capable of operating at temperatures up to 350°C. However, technological advances in jet-engine designs since the fifties have resulted a continuous need for stronger, lighter, and more temperature resistant materials for aircraft fabrication. [Ref. 2: p. 106]

The success of jet-engine fan and compressor components made of IMI318 resulted in most of the early research emphasis being placed on titanium aluminides with less than 10% aluminum by weight. [Ref. 1: p. 37] This research led to the production of the most advanced alloys available today, such as IMI829 (Ti-5.5Al-3.5Sn-3Zr-1Nb-0.25Mo-0.25Si) which is capable of operation at temperatures up to 600° C. In the past decade research emphasis has been shifted toward titanium alloys with high aluminum content, based on the two ordered intermetallics $Ti_3Al(\alpha_2)$ and $TiAl(\gamma)$ which maintain order up to their melting points thus showing excellent potential for aerospace applications at temperatures of 900° C. As shown in Table I, these alloys have high temperature properties comparable to nickel based alloys, but their inherent limited ductility at low temperatures has prevented cost effective fabrication to date [Ref. 1: p. 37] [Ref. 2: p. 106] [Ref. 4: p. 353].

TABLE I. PROPERTIES OF HIGH TEMPERATURE ALLOYS

Property	Ti Base	Ti_3Al	TiAl	Superalloys
Density (g/cm ³)	4.5	4.15-4.7	3.76	8.3
Young's Modulus (GN/m ²)	110-96	145-110	176	206
Max. Temp.-Creep (°C)	538	815	1038	1093
Max. Temp.-Oxidization (°C)	593	649	1038	1093
Ductility-Room Temp. (%)	.20	2-5	1-2	3-5
Ductility-Operating Temp. (%)	High	5-8	7-12	10-20

2. Current Research Emphasis

The need of aerospace industry for materials which can operate at temperatures above 600°C is driving the current research of how to solve the low temperature embrittlement problem of Ti₃Al and TiAl. As is observed in Lipsitt's 1985 overview of titanium aluminides, over a decade of research has not produced any one comprehensive solution to the problem. However, extensive information has been acquired concerning these ordered intermetallics [Ref. 4]. Data which may provide the key to the solution when combined with current studies. Among the topics of study are:

- Ternary alloying and dispersion strengthening [Ref. 2] [Ref. 5]
- Intermetallic alloying through powder mechanical alloying [Ref. 6] [Ref. 7]
- Deformation mechanisms of the intermetallic lattice [Ref. 8] [Ref. 9]
- Electronic structure of planar faults in intermetallics [Ref. 10] [Ref. 11]
- Phase transition characteristics and microstructural features [Ref. 12] [Ref. 13]
- Rapid solidification processing methods effects on microstructure. [Ref. 14]

B. MATERIAL CHARACTERISTICS

1. Microstructure

The first significant step in identification of γ TiAl and TiAl₃ came in 1951 when Ogden et al. produced a tentative phase diagram of the Ti-Al system based on their study of the 0 to 50% Al region and earlier studies which had been concentrated specifically on the aluminum rich alloy and the solubility of Titanium in aluminum [Ref. 15]. Murray produced the most current phase diagram as shown in Figure 1 [Ref. 16].

a. Characteristics of the TiAl Phase Diagram

The accuracy of Figure 1 is under dispute, especially for temperatures in excess of 1000°C [Ref. 12: p. 1322] [Ref. 17]. Of particular interest are the disputed compositions of 40 to 55 at.% Al; this region encompasses the ordered intermetallic α_2 -Ti₃Al (DO₁₉) and γ TiAl (L1₀) phases and their surrounding equilibrium phase fields: a cubic (A2) high temperature β -phase and a hexagonal (A3) α -phase. [Ref. 12: p. 1322]

Murray proposes for a Ti-50at.%Al the formation of cubic dendrites of β surrounded by γ -segregate from the peritectic reaction $L + \beta \rightarrow \gamma$. The β -phase then undergoes a solid-state transformation to ($\alpha_2 + \gamma$) at room temperature [Ref. 18]. Valencia, McCullough and others studied samples formed from a variety

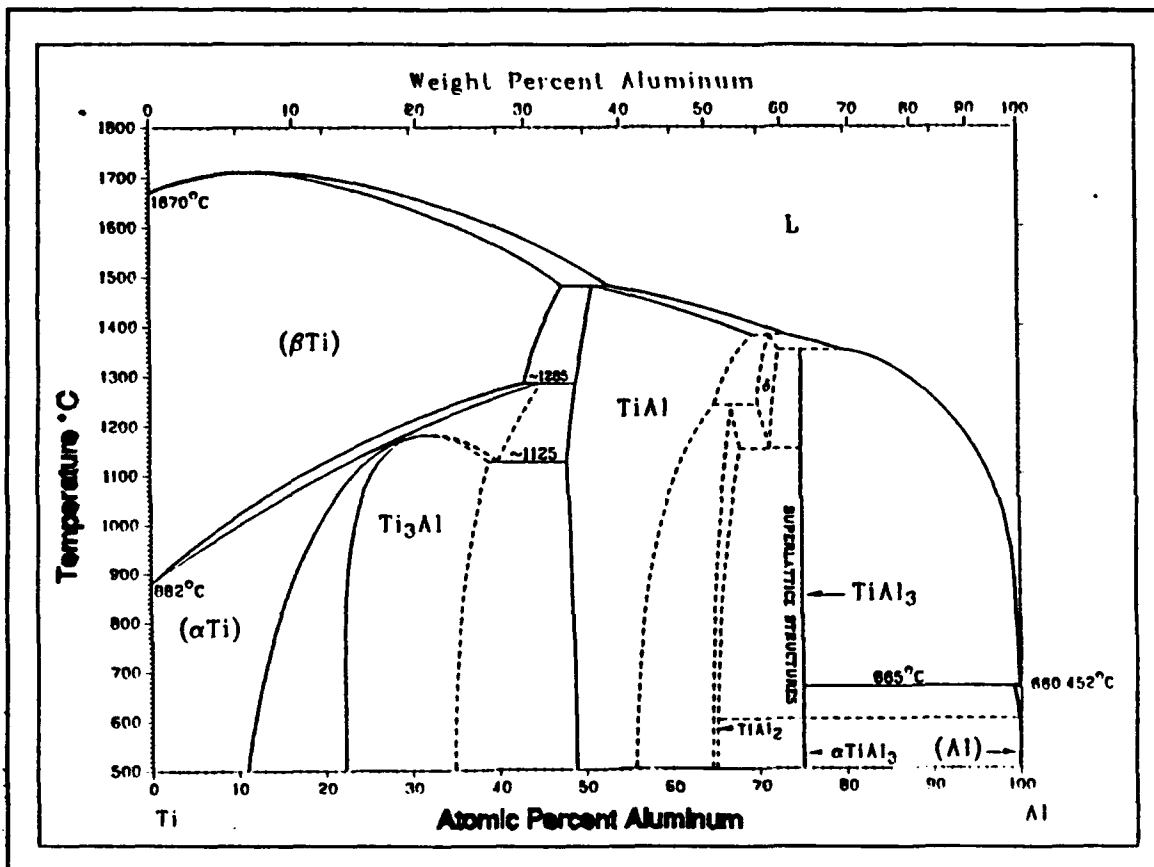


Figure 1. Ti-Al Phase Diagram

of solidification processes using SEM, TEM, and high temperature x-ray diffraction [Ref. 19]. They concluded that Murray's phase diagram needed revision to include a high temperature α -phase field in equilibrium with the liquid phase, as well as modifications to the $\alpha + \gamma$ field. Their proposed changes are shown as dotted lines on the disputed portion of Murray's phase diagram in Figure 2 [Ref. 20]. McCullough, et al's recommended changes agree with the earlier version of Willey and Margolin [Ref. 21].

McCullough et al. observed that for alloys in the range of ~49-55at.%Al, the primary hexagonal α dendrites form upon cooling from liquid (versus Murray's prediction of body center cubic β dendrites) and decompose in the following sequence: $\alpha \rightarrow \alpha_2 \rightarrow (\alpha_2 + \gamma)$. They also observed that for alloys of ~48-52at.%Al the α decomposition resulted in the formation of a cellular γ_c and the γ segregate which have no orientation relationship. In conclusion they stated that the solidification and solid state transformation of alloys in the ~49-55at.%Al range occurs in the following sequence [Ref. 12: p. 1335]:



Valencia et al. had proposed a similar but less detailed transformation prior that identified the instability of the α and complete stability of the γ during solidification process. [Ref. 19, p. 1343]

b. Crystallography

In 1952, Duwez and Taylor conducted a study of binary titanium aluminides with compositions of 46 to 62at.%Al. Their results which have held up to date are as follows:

- TiAl has a face-centered tetragonal $L1_0$ type structure (shown in Figure 3).
- The lattice parameter a decreases and the c increases with an increase in Al content due to the substitution of Al atoms for Ti resulting in expansion only in the basal plane.

- The c/a ratio increases from 1.017 to 1.026 for the 46 to 62at.%Al increase and the stoichiometric c/a is 1.02.
- It is probable that the c/a increase is related to the increase in electron concentration associated with addition of Al [Ref. 22: p. 71].

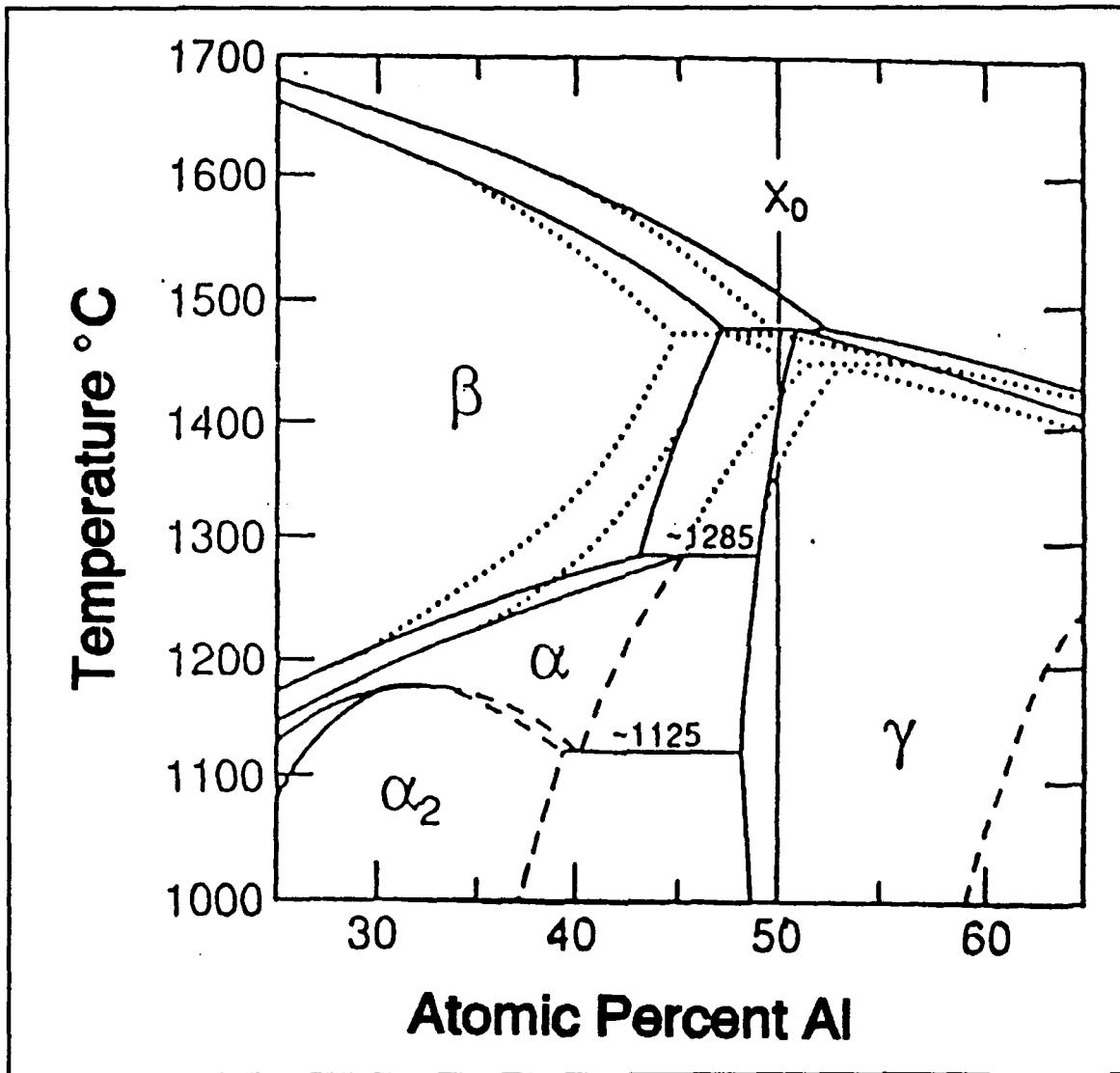


Figure 2. Proposed Revisions to Ti-Al Phase Diagram

Valencia et al. produced similar results in 1987, as did Cade in 1991. [Ref. 19: p. 1341] [Ref. 3: p. 40]

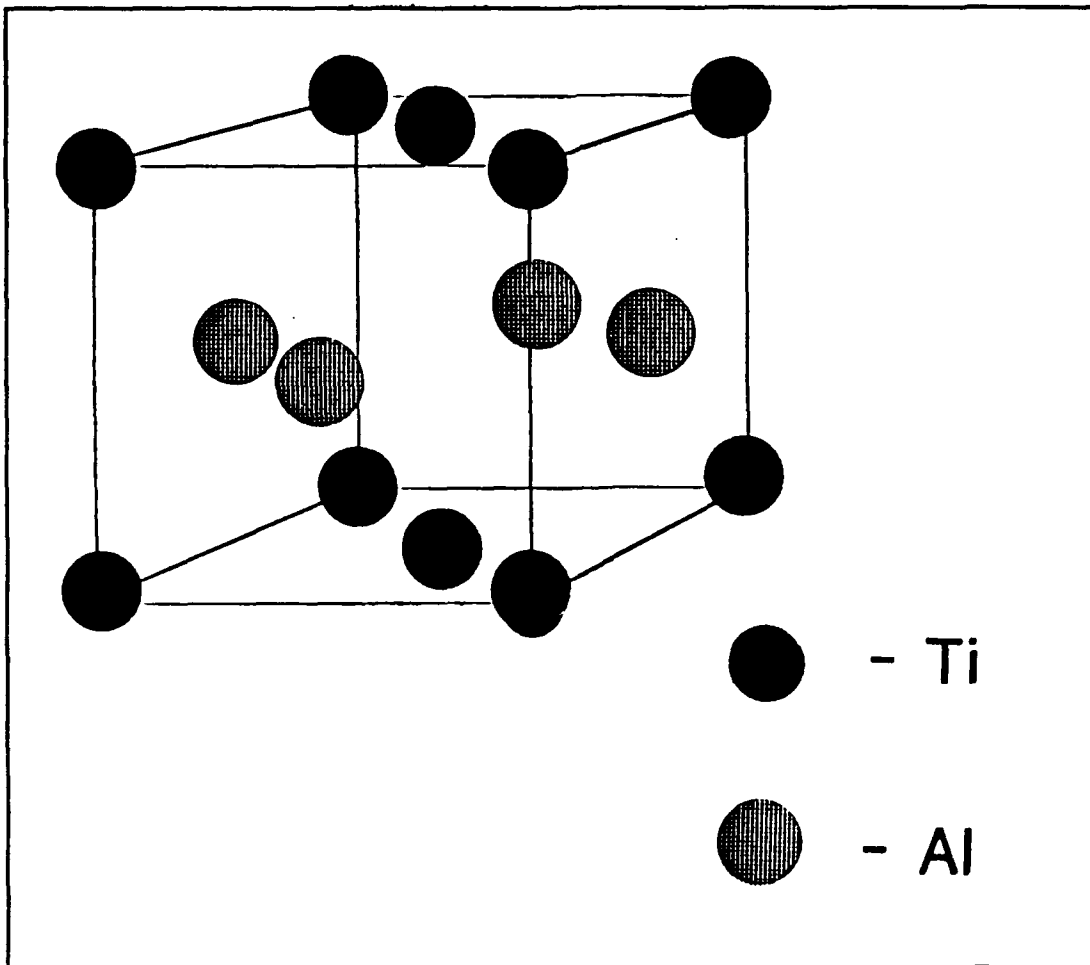


Figure 3. L₁₀ Face Centered Tetragonal TiAl Lattice Structure

Duwez and Taylor stated binary TiAl has an AuCu order after their early study, however, further research has established it to be a long range order which takes place during transformation from liquidus to solidus [Ref. 22: p. 71]. Li et al. studied the effects of rapid quenching on Ti-Al long range ordering and established that it was possible to shorten the long range order, but in doing so the

tetragonal distortion was altered, as well as plastic deformation behavior. In the course of the study it was observed that in aluminum rich off-stoichiometric Ti-Al alloy the predominant defect mode is antisite substitution [Ref. 23].

2. Strength and Ductility

a. Deformation Mechanisms

The earliest systematic research of flow stress and ductility for TiAl was conducted by Shechtman et al. and Lipsitt et al. [Ref. 24] [Ref. 25]. The compression tests of Shechtman et al. identified the expected $a/2[110]$ type dislocations and an unexpected "hard" slip mode $a/2[011]$ type which generated $a/6[112]$ partials that created numerous stacking faults related to the $[112] [111]$ twinning [Ref. 24: p. 1381]. Tensile data from the research of Lipsitt et al. is shown in Figure 4 along with that of Huang and Hall [Ref. 25] [Ref. 26].

The observed ductile to brittle transition temperature of 700°C is clearly evident. Lipsitt et al. determined the $a/6[112]$ partial dislocation which is a constituent of the $a[011]$ superdislocation controls the plasticity of TiAl and pinned below 600°C the possible Burger's vectors for TiAl are shown in Figure 5. The research also reported no disorder occurred up to 1000°C and that exposure to oxidizing conditions had no effect on tensile data [Ref. 25: p. 1996].

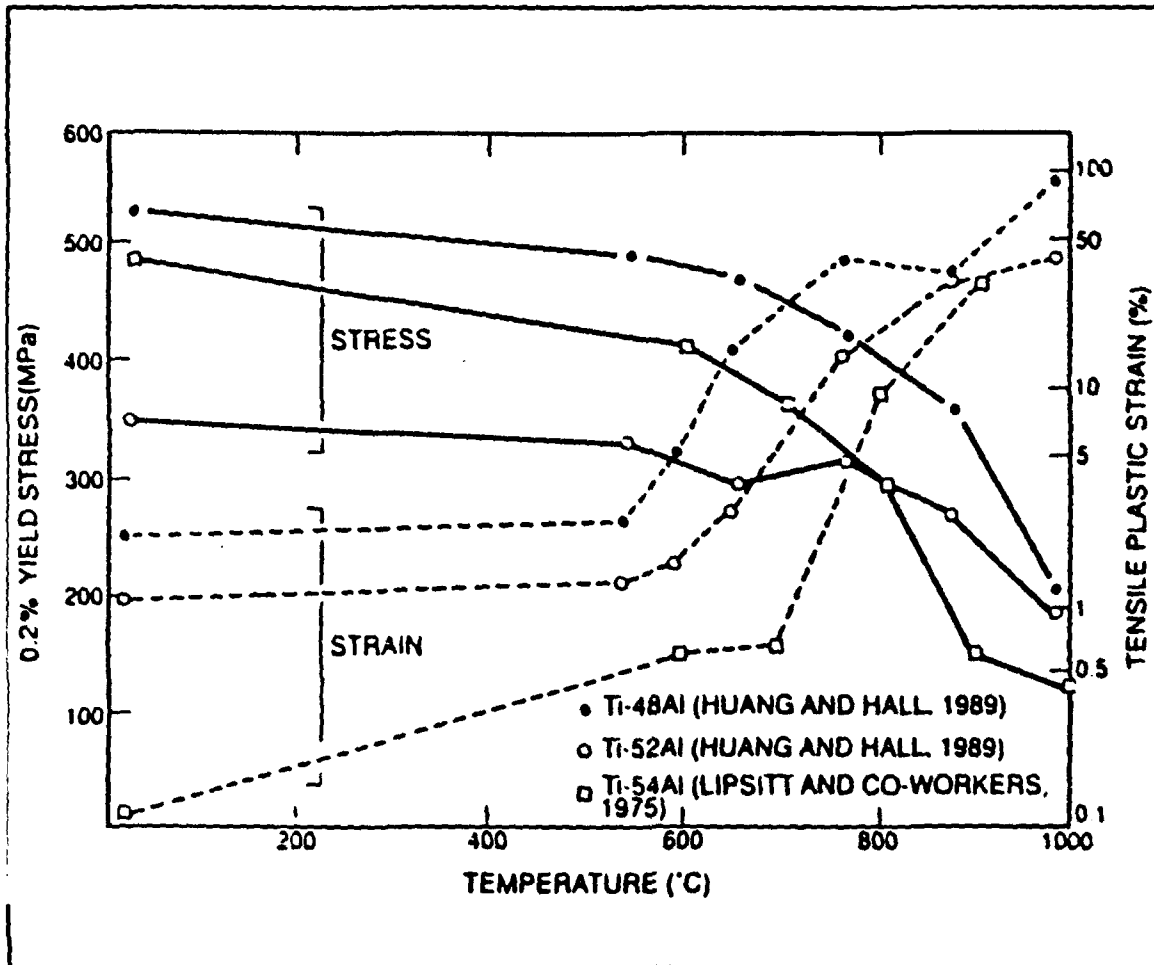


Figure 4. Tensile Test Data

Numerous researchers conducted follow on investigations of the immobilization of the $a/2[112]$ partial and its effect on twinning. Among these proposed reasons for the pinning were:

- Superdislocations are pinned by jogs of faulted dipoles which increase the obstacles for dislocation motion [Ref. 27: p. 64].
- A Kear-Wilsdorf mechanism operates in which screw superdislocations are immobilized by cross-slip on to a cube plane [Ref. 28].

- Increased electron charge densities with addition of aluminum leads to anisotropy near titanium atoms which results in entrapment of dislocations in Peierls stress valleys. The deep valleys cause the $a/2[110]\{111\}$ to be essentially sessile (extrinsically faulted dipoles) at room temperature [Ref. 29: p. 862].
- Peierls stress is higher at low temperatures and dislocation motion is inhibited. At high temperatures the Peierls stress decreases and the $a/1[110]\{111\}$ dislocations significantly contribute to the strain thus improving ductility [Ref. 9: p. 157].

Additionally, Feng et al. have identified other types of twins in TiAl alloys and shown the need for further research of twinning, an important deformation mode in ordered intermetallics [Ref. 30][Ref. 31].

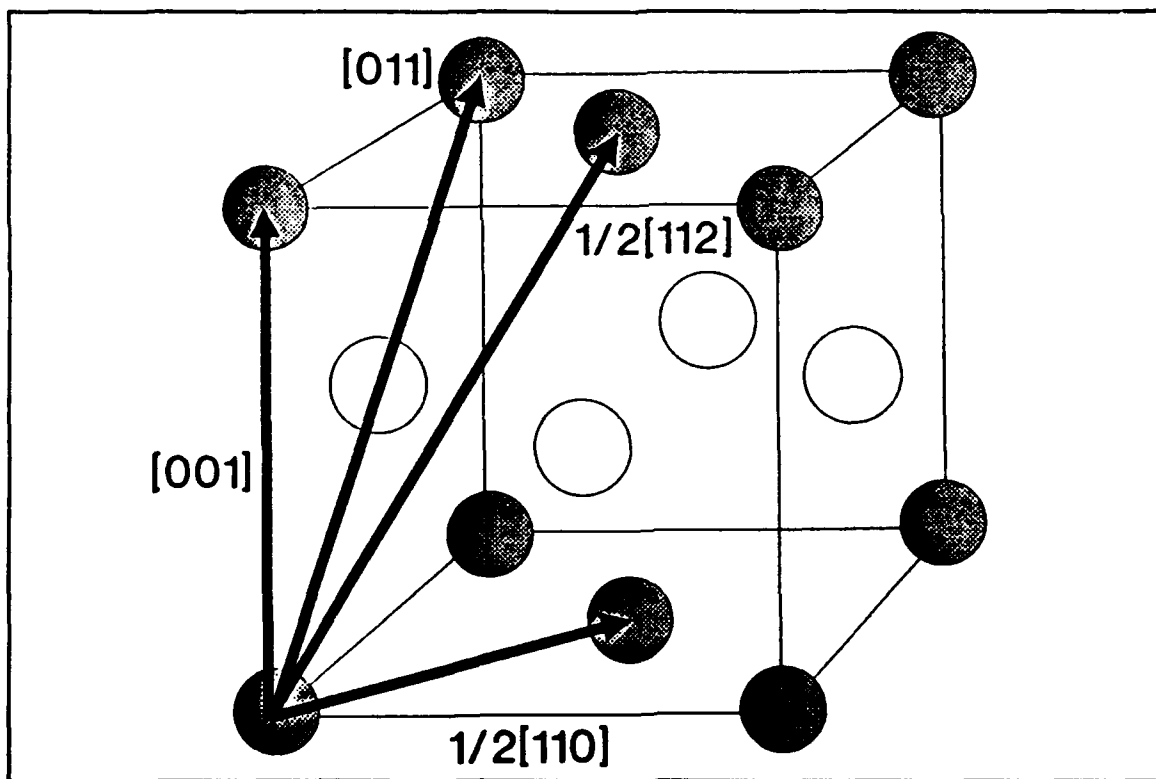


Figure 5. Possible Burger's Vectors of TiAl

b. Effects of Alloying

Many alloying studies have been conducted on TiAl in an attempt to improve ductility at low temperatures. Yamaguchi and Umakoshi produced an excellent overview of the TiAl alloying research concerned with ten elements, a summary is as follows [Ref. 8: pp. 83-87]:

(V) The addition of vanadium to compounds with the TiAl/Ti₃Al two-phase structure improved ductility; a 2% elongation at room temperature was accomplished with a compound of Ti-48at.%Al-1at.%V. The replacement of 10% of Ti and Al through substitution in Ti₄₅Al₅₅ is expected to produce similar results to the two phase, but substitution of only the Ti results in increased yield stress and decreased compression strain. Thus V addition for Al rich TiAl may not be beneficial.

(Mn) The addition of manganese decreases the c/a ratio and improves the ductility of two phase compounds. As in alloying with V, the elongation is near 2%. The cause for this improvement may be improved microstructure and/or increased deformation twinning activity.

(Cr) Research has shown that chromium addition may improve plasticity for compounds of TiAl/Ti₃Al two-phase structure. However, it has no effect on single-phase, Al rich compositions.

(Nb, Hf, Ta, and W) These elements normally replace Ti atoms and reduce the ductility. Nb and Ta increase the resistance to oxidation. None of the elements produce positive low temperature deformation effects in single-phase TiAl.

(Mo) Two percent elongations in Ti rich compounds have been produced through the addition of molybdenum. Fine equiaxed grains were produced and superplasticity could be observed at 800°C.

(Ga) Solution softening was accomplished by maintaining 50 at.%Ti and substituting Al atoms with 5 at.% gallium. However, no room temperature data was available.

(O) Normal oxygen content for TiAl ingots is 0.04-0.1 wt.%O. Decreasing the oxygen content can significantly reduce its solution hardening effects, as well as, changing the volume fraction and aluminum content which improves ductility. Controlling oxygen content is very difficult and no comprehensive studies have been completed on use or avoidance in TiAl alloying.

3. Methods of Analysis

To better understand the deformation modes of TiAl and possibly improve its low temperature ductility, a complete study of interatomic bonding mechanisms is necessary. Woodward et al. have produced mathematical models for the theoretical electron distribution of TiAl. The charge density [milli-electrons/(bohr radius)³] contours shown in Figure 6 clearly represent the strong

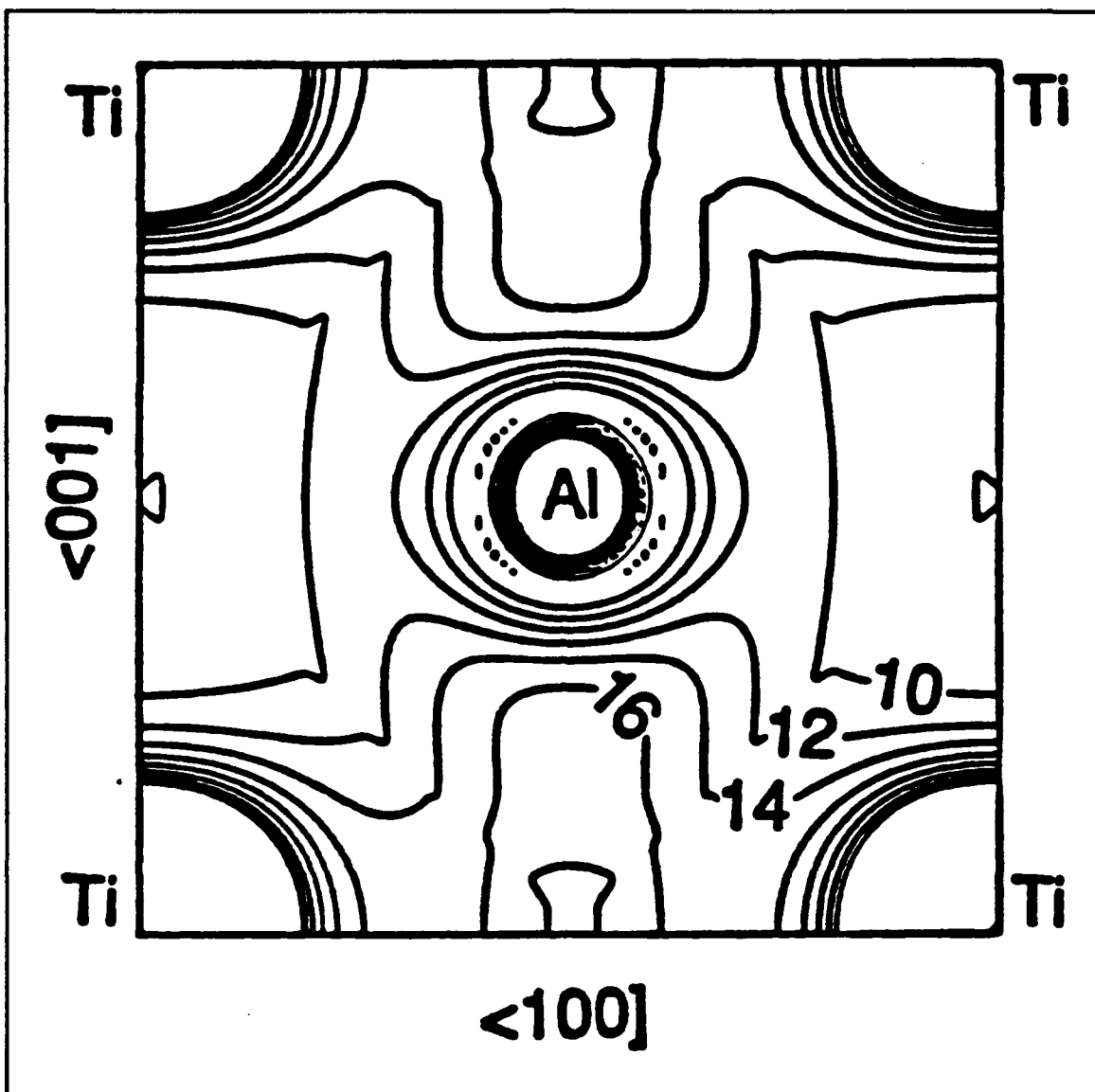


Figure 6. Charge Density Contour of L1₀ TiAl (100) Plane

Ti-Ti bonding and lower energies of the interstitial sites and Ti-Al bonds [Ref. 10].

Experimental electron charge distribution can be determined using by implementing

a Fourier sum and accurately measured structure factors as follows:

$$\rho(x,y,z) = \frac{1}{\Omega} \sum_h \sum_k \sum_l F_{hkl} \exp[2\pi i(hx+ky+lz)] \quad (1)$$

where $\rho(x,y,z)$ is the electron density; (x,y,z) is the position in the unit cell; Ω is the volume of the unit cell; F_{hkl} is the structure factor; and $h, k,$ and l are the Miller indices [Ref. 32: p. 671].

The following is a brief summary of methods for accurately measuring structure factors:

a. X-ray Pendellösung Measurement

Based on the dynamical theory of X-ray diffraction, Pendellösung fringe spacings can be measured to determine experimental structure factor. A large single crystal and collimation of characteristic x-rays are used to produce a diffraction phenomena known as a Pendellösung fringe. The fringes are produced by the change in extinction distances associated with different wavelengths of radiation. The extinction distance is a function of the structure factor; thus structure factors can be determined using fringe spacings of different wavelengths. An x-ray diffractometer may be used by measuring the fringe spacing of a single wavelength at varying angles of diffraction [Ref. 33]. Structure factor accuracies of $\pm 0.1\%$ have been obtained using this procedure [Ref. 32].

b. *γ-ray Diffraction*

γ-ray diffraction is very comparable to x-ray diffraction however, gamma radiation has a shorter wavelength than X-radiation thus produces better penetration with less extinction and dispersion effects. Accuracies of $\pm 0.2\%$ have been obtained [Ref. 32].

c. *Electron Diffraction*

The most accurate method of determining structure factor using a transmission electron microscopy is the critical voltage method. This method uses a sample thick enough to produce sharp Kikuchi lines (usually $\geq 1000\text{\AA}$). The sample is set the Bragg condition and a critical electron acceleration voltage is determined by observing the the diffracted beam intensity of second order or higher reflections which is very small due to destructive interference. The critical voltage is very sensitive to the crystal potential for systematic row concerned thus can be used to determine structure factors with accuracies of $\pm 0.1\%$, but only at low angles [Ref. 34].

d. *X-ray Diffraction*

The least accurate of the methods mentioned here, powder x-ray diffraction (XRD) is only capable of producing structure factor accuracies of $\pm 0.5\%$. However, it has the advantages of not requiring a single crystal specimen, full use of the Bragg angle spectrum, and is capable of measuring both fundamental and

superlattice reflections. Thus, it is the mostly commonly used method for measuring structure factors and lattice parameters which maybe readily calculated using diffracted peak positions. Cooper [Ref. 35] and Hughes et al. [Ref. 36] have produced excellent results using powder x-ray diffraction methods to determine the Debye-Waller factors of NiAl; and it will be used for the present study of TiAl.

C. FUNDAMENTALS OF X-RAY DIFFRACTION

1. Bragg's Law

Bragg explained x-ray diffraction effects in terms of "reflection from a stack of parallel atomic planes" and demonstrated that when an incident beam of x-rays strikes an extended crystal face it "reflects" in accordance with the following equation:

$$n\lambda = 2d\sin\theta \quad (2)$$

where n is the number of interplanar spacings, λ is the wavelength of x-ray beam, d is the interplanar spacing, and θ is the reflection angle.

The lines pp , p_1p_1 , p_2p_2 of Figure 7 [Ref. 37: p. 131] represent traces of a series of atomic planes parallel to the crystal face with a constant interplanar spacing d which for the $L1_0$ (face centered tetragonal lattice) structure of γ TiAl is calculated using the following equation:

$$\frac{1}{d} = \sqrt{\frac{h^2 + k^2}{a_o^2} + \frac{l^2}{c_o^2}} \quad (3)$$

where h , k , and l are the Miller indices of the planes a_o and c_o are the lattice parameters [Ref. 38: p. 47]. Incident x-rays AB and $A'B'$ of wavelength λ impinge on the planes and bounce off in the direction of CD . Bragg's law is only satisfied when the reflected wavelet from B' arrives at C in phase with wave ABC , thus reinforcing ABC through constructive interference and a reflection will occur [Ref. 37: p. 131].

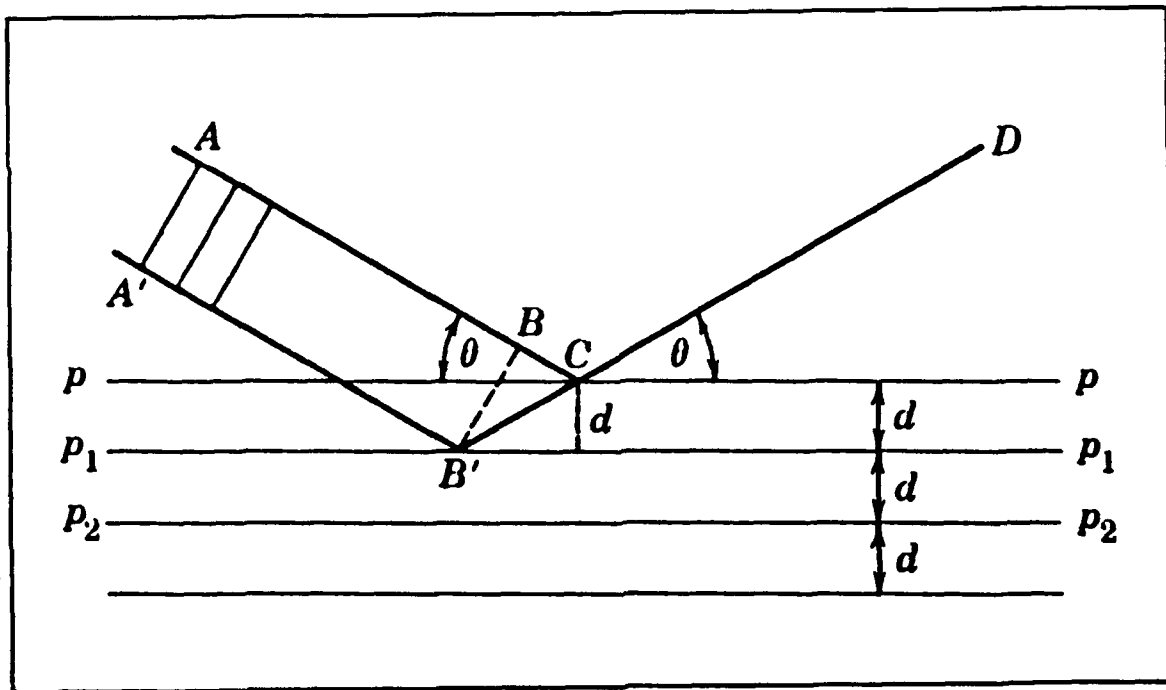


Figure 7. Bragg's Law Geometry

The diffracted x-ray intensities are recorded by placing an x-ray detector at D. Normally the incident beam axis is fixed and the sample and detector are moved θ and 2θ respectively. The detected diffraction intensities are processed and plotted versus Bragg angles (2θ). Figure 8 [Ref. 37: p. 284] shows a $K\alpha_1\alpha_2$ reflection peak. The integrated intensities of each peak can be calculated by measuring the area under the curve and subtracting the associated background area corresponding with background intensities on each side of the peak. Note, the doublet in Figure 8 is two overlapping peaks produced by the similarity in $K\alpha_1$ and $K\alpha_2$ wavelengths for copper radiation.

2. Diffraction Intensity Calculations

Theoretical intensities for powder x-ray diffraction are calculated using the following equation:

$$I=K|F|^2p\phi(\theta)\exp^{-2M} \quad (4)$$

I is the integrated intensity, K is the constant of proportionality (associated with the equipment used in the experiment), F is the structure factor, p is the multiplicity factor, $\phi(\theta)$ is the Lorentz-Polarization factor, and M is the temperature factor.

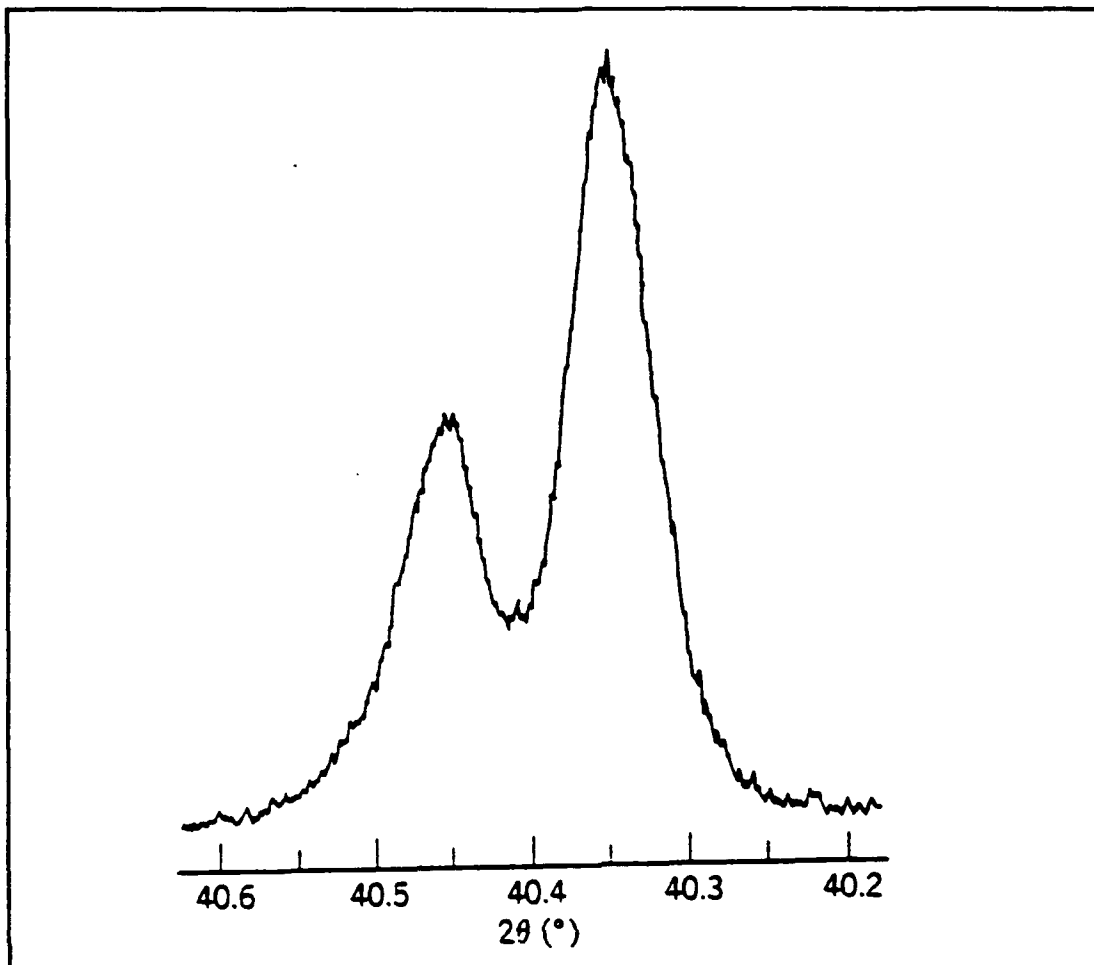


Figure 8. Intensity Peak with $K\alpha_1\alpha_2$ Doublet

a. Structure Factor

Material structures are composed of repetitive fundamental unit cells. Each unit cell has a fixed atomic arrangement allowing calculations for the entire structure using the x-rays diffracted by one unit cell. The amplitude of x-ray energy diffracted by the unit cell relative to that diffracted by a single electron equals the structure factor. Assuming Bragg's law is satisfied for an incident beam to reflect, the location (uvw) of the individual atoms within the unit cell can be determined by

recording diffracted intensities as a function of the Bragg angle. This is accomplished with the understanding that as Bragg angle changes the atomic planes, atoms interacting in the reflection change. The amplitude of x-ray energy diffracted by the unit cell relative to that diffracted by a single electron equals the structure factor. Since the amount of energy reflected by the unit cell is a function of that reflected by each individual atom within the cell, the structure factor can be calculated as follows:

$$F_{hkl} = \sum_N f_n \exp[2\pi i(hu_n + kv_n + lw_n)] \quad (5)$$

Where N is the total atoms in the unit cell, n is the atom type, f is the atomic scattering factor (discussed in further detail later), hkl are the Miller indices, and uvw are the corresponding atomic position within the unit cell. For γ TiAl, Equation 5 can be reduced to:

$$F_F = 4(m_{Ti}f_{Ti} + m_{Al}f_{Al}) \quad (6)$$

for the fundamental reflection (hkl all odd or all even) and:

$$F_S = 4m_{Ti}(f_{Ti} - f_{Al}) \quad (7)$$

for the superlattice reflections (hkl mixed), by assuming γ TiAl of m_{Ti} at.% has Ti atoms at uvw equals 000 and $\frac{1}{2}\frac{1}{2}0$ and Al at $0\frac{1}{2}\frac{1}{2}$ and $\frac{1}{2}0\frac{1}{2}$. [Ref. 37: p. 120]

b. Atomic Scattering Factor

The atomic scattering factor is used to describe the "efficiency" of scattering of a given atom in a given direction. It is equal to the amplitude of the wave scattered by an atom relative to that of one electron. The atomic scattering factor equals the atomic number (Z) for $\theta=0$. For a given wavelength of radiation, the waves scattered by the atom's individual electrons become increasingly out of phase as θ increases, thus decreasing the scattering factor [Ref. 38: p. 112]. Anomalous dispersion occurs when the wavelength of the incident radiation is very near that of the absorption edge for the scattering atom and the real ($\Delta f'$) and imaginary ($\Delta f''$) corrections must be applied as follows [Ref. 38: p. 113]:

$$f=f_o+\Delta f'+\Delta f'' \quad (8)$$

Atomic scattering factors (f_o) as well as corrections for anomalous dispersion ($\Delta f'$, $\Delta f''$) are tabulated in the International Tables for X-Ray Crystallography [Ref. 39].

c. Multiplicity Factor

Many atomic planes can contribute to the same reflection in powder diffraction resulting in increased intensities for a single family of planes. The value of the multiplicity factor (p) depends on the crystal system. For the tetragonal crystal form of γ TiAl, the multiplicity factor for the $\{111\}$ plane is 8. The (100) and (001) planes do not have the same spacing so p for the $\{100\}$ plane is 4, while it is 2 for the $\{001\}$ [Ref. 38: p. 127].

d. Lorentz-Polarization Factor

The Lorentz-Polarization factor ($\phi(\theta)$) combines the corrections for number favorably oriented crystals, variation of intensity in the vicinity of the Bragg angle, geometry of the reflection, and polarization. The factor is expressed as a function of the θ as follows:

$$\phi(\theta) = \frac{1 + \cos^2 2\theta}{\sin^2 \theta \cos \theta} \quad (9)$$

e. Temperature Factor

Atoms are assumed to be at fixed positions for the atomic scattering factor. However, atoms undergo thermal vibrations about their mean positions even

at a temperature of absolute zero. As temperature increases the amplitude of the vibration increases thus producing three main effects [Ref. 38: p. 135]:

- The lattice parameters of the unit cell expands, causing a change in interplanar spacing (d) and therefore shifting the Bragg angle of the diffracted lines.
- Diffracted intensities decrease.
- The background intensity increases as seen in Figure 9 [Ref. 38: p. 138].

At high- θ the reflections involve low interplanar spacings so the increased amplitudes of vibration associated with high temperature result in significant degradation in diffracted intensities as seen in Figure 9. In intensity calculations this effect is corrected by introducing the temperature factor e^{-2M} [Ref. 38: p. 136] where M is calculated as follows:

$$M = B \frac{\sin^2 \theta}{\lambda^2} \quad (10)$$

B is the temperature dependent Debye-Waller factor for monatomic cubic crystals and is calculated as follows [Ref. 37: p. 145]:

$$B = \frac{6h^2}{m_d k \theta_D} \left[\frac{\phi(x)}{x} + \frac{1}{4} \right] \quad \text{where } x = \frac{\theta_D}{T_{ATM}} \quad (11)$$

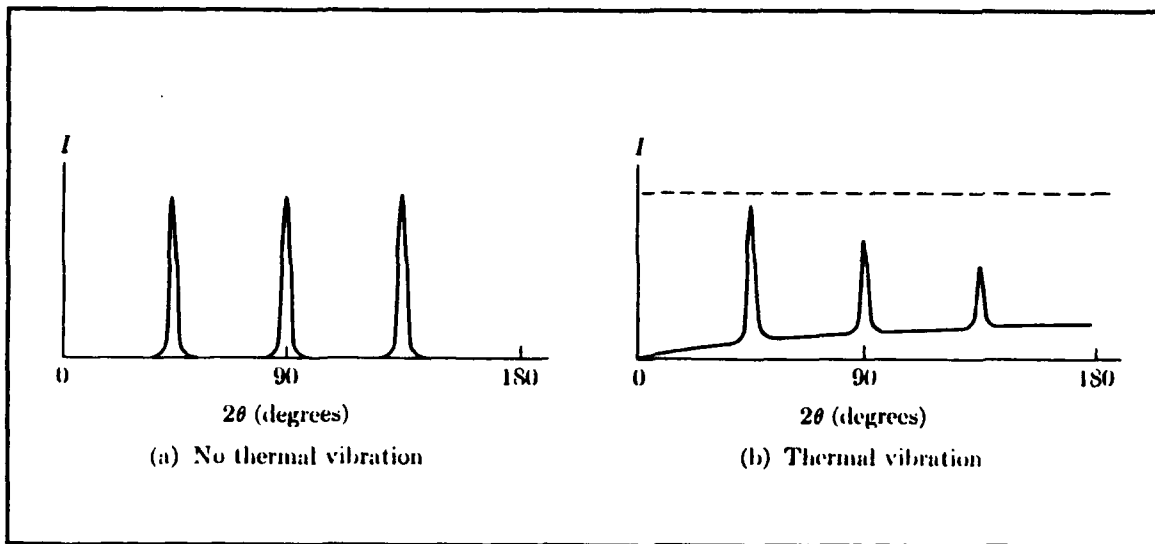


Figure 9. Effect of Thermal Vibration.

T_{atm} is the atmospheric temperature in degrees Kelvin. μ is the atomic weight. θ_D is the Debye characteristic temperature which is calculated as follows for cubic elements [Ref. 40]:

$$\theta_D = \frac{1}{X} \sqrt{\frac{1800T_m}{\mu a^2}} \quad (12)$$

X is the atomic r.m.s. amplitude at the melting point expressed as a fraction of the Wigner-Seitz radius, a dimensionless constant ranging from 0.2 to 0.25 for most solids. T_m is the melting point in degrees Kelvin and a is the lattice parameter. $\phi(\theta_D/T_{\text{atm}})$ is the Debye function which is calculated as follows [Ref. 37, p. 145]:

$$\phi(x) = \frac{1^x}{x_0} \int \frac{\xi d\xi}{e^\xi - 1}; \quad x = \frac{\theta_D}{T_{atm}} \quad (13)$$

Both θ_D and $\phi(\theta_D/T_{atm})$ are tabulated in the *International Tables* [Ref. 41] and [Ref. 42].

In a $L1_0$ tetragonal lattice each atom's thermal motion is represented by an ellipsoid of vibration and the corresponding Debye-Waller factors are designated $B_{Ti(c)}$ and $B_{Al(c)}$ for planes perpendicular to the c axis and $B_{Ti(a)}$ and $B_{Al(a)}$ for planes perpendicular to the a axis [Ref. 43]. To calculate the B for planes lying in between the c and a axes the simple equation of an ellipse is used where $B_{Ti(c)}$ and $B_{Al(c)}$ are the major axes and $B_{Ti(a)}$ and $B_{Al(a)}$ are the minor. The ellipsoid of vibration for a Ti atom is shown in Figure 10.

When the Debye-Waller factors of the individual atom types present are included in the structure factor calculations for TiAl, the following equations result:

$$F_F = 2(m_{Ti}f_{Ti}\exp(-B_{Ti}\frac{\sin^2\theta}{\lambda^2}) + m_{Al}f_{Al}\exp(-B_{Al}\frac{\sin^2\theta}{\lambda^2})) \quad (14)$$

for the fundamental reflections (hkl all odd or all even) and

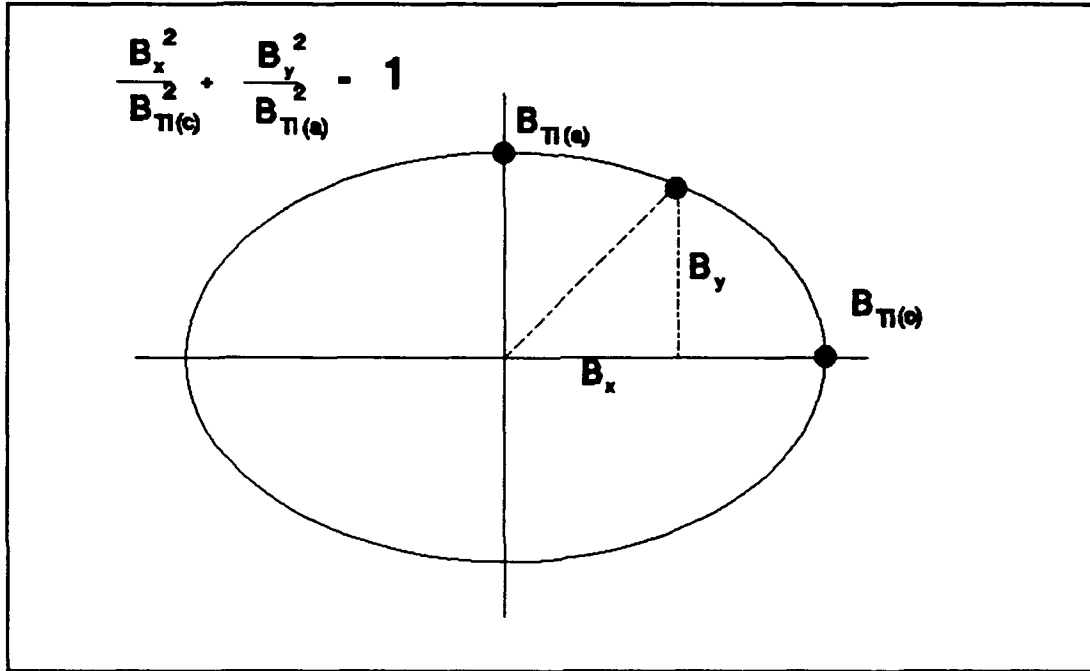


Figure 10. Ti Ellipsoid of Thermal Vibration

$$F_S = 4m_{Ti} \left(f_{Ti} \exp\left(-B_{Ti} \frac{\sin^2 \theta}{\lambda^2}\right) - f_{Al} \exp\left(-B_{Al} \frac{\sin^2 \theta}{\lambda^2}\right) \right) \quad (15)$$

for the superlattice reflections (hkl mixed).

At high temperatures near the Debye temperature nearest-neighbor force constants dominate the Debye-Waller factors and the c/a ratio is close to 1 so that $B_{Ti} \approx B_{Al}$ is likely to be a reasonable approximation so that Equations 14 and 15 become [Ref. 32]:

$$F_F = 2(m_{Ti} f_{Ti} + m_{Al} f_{Al}) \exp\left(-\bar{B} \frac{\sin^2 \theta}{\lambda^2}\right) \quad (16)$$

and

$$F_S = 4m_{Ti}(f_{Ti} - f_{Al})\exp\left(-\bar{B}\frac{\sin^2\theta}{\lambda^2}\right) \quad (17)$$

where

$$\bar{B} = \frac{B_{Ti} + B_{Al}}{2} \quad (18)$$

For γ TiAl at room temperature this may be a reasonable approximation as a calculation from melting point data indicates that the Debye temperature for this alloy is around 359° K.

3. Lattice Parameter Calculations

Extremely accurate lattice parameter calculations can be made by plotting the lattice parameter corresponding to diffraction peak positions versus the Nelson-Riley using the Equations 19 and 20.

$$\text{lattice parameter} = \frac{\lambda\sqrt{h^2+k^2+l^2}}{2\sin\theta} \quad (19)$$

$$\text{Nelson-Riley function} = \frac{\cos^2\theta}{\sin\theta} + \frac{\cos^2\theta}{\theta}; \quad \theta \text{ in radians} \quad (20)$$

The Nelson-Riley function approaches zero as θ goes to $\pi/2$ radians. For tetragonal crystals, the value of a is calculated for all $hk0$ reflections and value of c for all $00l$ reflections. The resulting lines are curve fit using a method of least squares and values for a_0 and c_0 are extrapolated for $\theta = \pi/2$. [Ref. 38: pp. 356-357]

4. Debye-Waller Temperature Factor

It is difficult to calculate accurate theoretical values for the temperature factor. Thus, experimental values for the Debye-Waller factor are made using the Wilson method which says if

$$I' = \frac{I_{\text{exp}}}{p\phi(\theta)|F|^2} \quad (21)$$

where I_{exp} is the experimental value of diffracted intensity, then

$$I' = K \exp\left[-2B \frac{\sin^2\theta}{\lambda^2}\right] \quad (22)$$

and taking the natural logarithm of Equation 22, results in the following linear equation:

$$\ln I' = \ln K - 2B \left[\frac{\sin^2\theta}{\lambda^2} \right] \quad (23)$$

When $\ln I'$ is plotted versus $\sin^2\theta/\lambda^2$ for each diffraction peak and the resulting line is curve fit using a method of least squares the slope of the line is equal to $-2B$ and the intercept equals $\ln K$. Due to extinction at low angles only high data points should be included when using the Wilson method.

5. Causes of Diffraction Peak Error

a. Peak Position Error

Diffractometer misalignments, curved specimen surfaces, improper sample thickness, displacement of sample from diffractometer axis, and vertical divergence of the incident beam can all lead to large inaccuracies in 2θ . Error can be minimized by calibration of diffractometer, proper sample preparation, and extrapolation of data recorded versus $\cos^2\theta$. [Ref. 38: pp. 359-360]

b. Peak Broadening Effects

Not actually an error, peak broadening can be an inconvenience due to line overlap. Fine particle sizes ($< 1000\text{\AA}$) and/or nonuniform microstresses within the powder particles will produce extensive line broadening. This can be avoided by maintaining powder particle sizes above $0.1\mu\text{m}$ and removal of residual stresses through annealing [Ref. 38: pp. 284-286].

c. Intensity Error

(1) *Preferred Orientation.* Each powder particle normally has a different crystallographic orientation from that of its neighbor. When the particles tend to cluster or orient toward some fixed reference frame, this preferred orientation results in falsely high or low diffracted intensity measurements due to the non-random orientation. The easiest way to prevent preferred orientation is by using fine powder particle sizes, thus the randomness of the crystallites. [Ref. 38: pp. 368-369]

(2) *Absorption and Extinction.* When an incident beam of radiation impinges on a crystal, it experiences a small but finite loss of energy with each successive atomic plane it passes through. This behavior is expressed by the following equation:

$$I = I_0 e^{-\mu x} \quad (24)$$

where I is the intensity transmitted, I_0 is the original incident beam intensity, e is the Napierian base, x is the thickness of the absorption layer in centimeters, and μ is the linear absorption coefficient [Ref. 37: p. 120].

During a Bragg reflection the incident beam experiences extraction and reflection of a small amount of energy with each successive plane it

passes, thus becoming significantly weaker as it passes to lower and lower planes. In addition, some of the reflected wavelets result in destructive interference caused by out of phase wavelet reflections off higher atomic planes back along the incident wave path. The net effect of these two phenomena is called extinction and for an "ideally perfect" crystalline structure its effect combined with absorption would prevent any detectible diffraction intensities at Bragg conditions [Ref. 37: pp. 139-140].

All real crystals have a mosaic structure and Equation 4 was derived on the basis of an "ideally imperfect" crystal which has no extinction and thus maximum reflecting power, due to complete misorientation of its small (0.1 μm to 1 μm) mosaic blocks. Neither ideally perfect, nor imperfect real crystals exist; and the desired effect of maximizing reflection power and while minimizing extinction can best be achieved by using a specimen with a small powder particle size [Ref. 37: p. 140]. The increasing effect on average observed intensity with increasing crystallite sizes can be seen in Table II where the mean integrated intensity of the sub 5 μm powder is 32.66% higher than that of the 15 to 50 μm [Ref. 37: p. 366].

Table II. INTENSITY MEASUREMENTS ON DIFFERENT SIZE FRACTIONS OF <325 - MESH QUARTZ POWDER

Specimen No.	15 to 50 μ Fraction	5 to 50 μ Fraction	5 to 15 μ Fraction	<5 μ Fraction
1	7612	8688	10841	11055
2	8373	9040	11336	11040
3	8255	10232	11046	11386
4	9333	9333	11597	11212
5	4823	8530	11541	11460
6	11123	8617	11336	11260
7	11051	11598	11686	11241
8	5773	7818	11288	11428
9	8527	8021	11126	11406
10	10255	10190	10878	11444
Mean Area	8513	9227	11268	11293
Mean deviation	1545	929	236	132
Mean percentage deviation	18.2	10.1	2.1	1.2

(3) *Intensity Scatter.* If a flat diffractometer specimen is held stationary during measurement of a diffraction peak, the number of properly oriented crystallites below 50 μ m in size which contribute diffracted rays to the peak is too small to yield a reproducible and true average intensity. The variations in ten separate intensity for five different crystallite size ranges are listed in Table II.

For the largest size the mean deviation in measured intensity is 18.2 percent whereas for the sub $5\mu\text{m}$ it is only 1.2 percent. These results can be mathematically predicted and a plot of deviation in diffraction intensities for various crystallite sizes and linear absorption coefficients is shown in Figure 11 [Ref. 37: pp. 365-367]. On examination of Table II and Figure 11, it is clearly evident that in order to reduce extinction and improve accuracy powder particle sizes for analysis in a powder x-ray diffractometer should be below 5 micron.

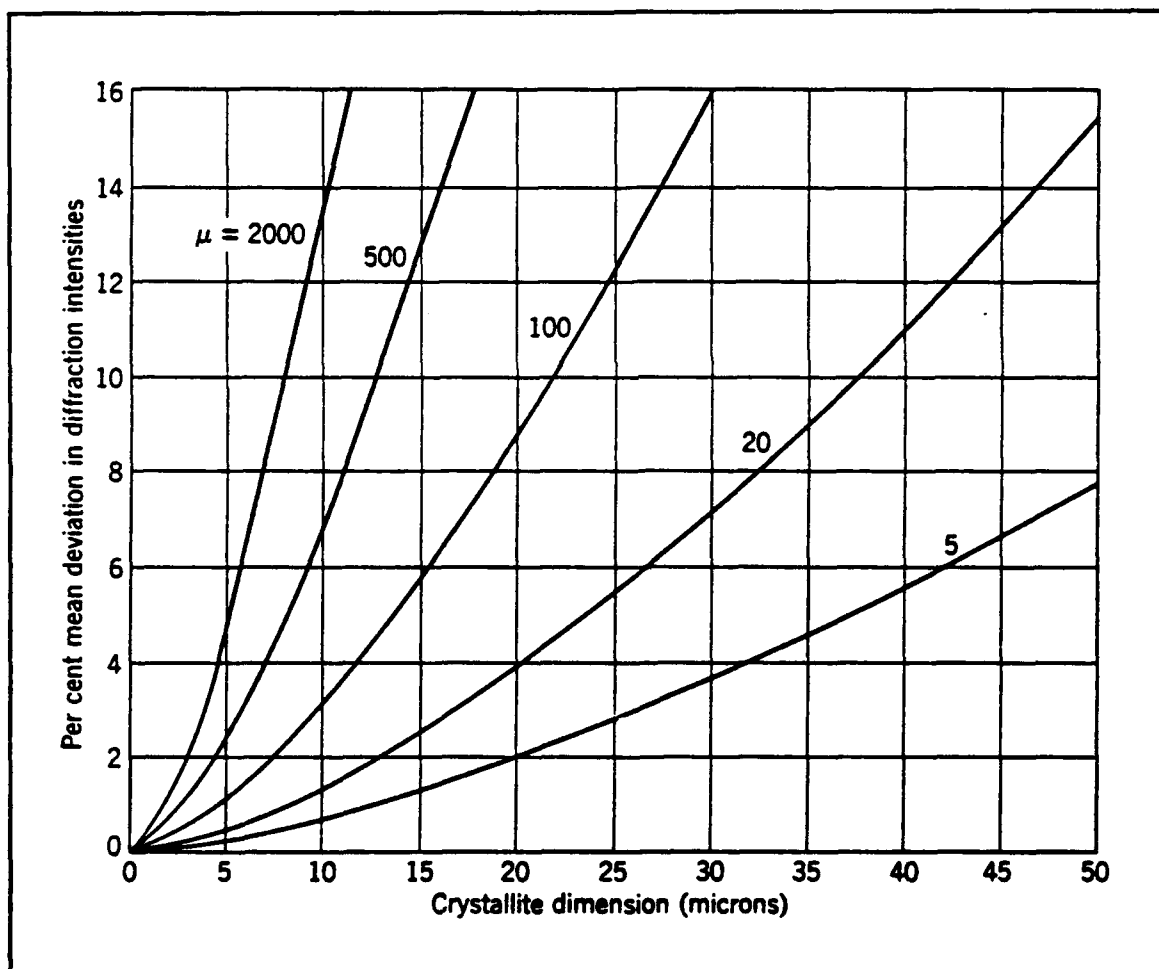


Figure 11. Intensity Deviations Associated with Crystallite Size

D. SCOPE OF PRESENT WORK

Lattice parameter measurements of γ TiAl were measured by Duwez and Taylor in 1952, using Debye-Scherrer camera [Ref. 22]. Cade measured the lattice parameters and structure factor using powder x-ray diffraction procedures and determined the Debye-Waller temperature factor, however, his measured intensities were significantly affected by extinction at low angles of reflection [Ref. 3]. The present research will use a smaller particle sized powder as a follow on to Cade's investigation of the lattice structure of the ordered intermetallic Ti-51at%Al, to include:

- Preparation of extinction free (sub 5 μ m) particle size powder using an acoustic sieving method.
- Accurate lattice parameter and structure factor measurement using powder x-ray diffraction procedures.
- Measurement of integrated intensities and determination of Debye-Waller temperature factors with comparison to melting point data and characteristic temperature.
- Verification of Cade's work and comparison of extinction effects due to powder particle size.

III. EXPERIMENTAL PROCEDURE

A. ALLOY COMPOSITION AND HEAT TREATMENT

A Wright-Patterson Air Force Base Materials Research Laboratory specimen of as-cast, Ti-51at%Al alloy was homogenized at 1200°C and furnace cooled to room temperature. The specimen was then sealed in a silica tube, backfilled with argon, reheated to 1200°C, and water quenched to room temperature; thus ensuring a single phase γ TiAl alloy. Analysis by source prior to heat treatment indicated an oxygen content of approximately 700 ppm by weight.

B. POWDER PREPARATION

1. Powdering

The surface oxide layer of the ingot was removed by grinding the specimen using 240 grit silicon carbide paper. Extreme hardness at room temperature prevented powder formation using the traditional filing method, therefore, lathe turnings were produced using a tungsten carbide bit. The specimen turnings were then pulverized to a fine powder using a ceramic mortar and pestle.

2. Sieving

Initially, all of the powder was passed through a U.S. Standard #400 (38 micron) sieve mesh. Then after extensive grinding with mortar and pestle the powder was placed in the acoustic sieve assembly shown in Figure 12. The powder was passed through 1500 line per inch (lpi) (10-11 micron) and 2000 lpi (5-7 micron) meshes sequentially with the sieve shown in Figure 13 at the highest power and frequency setting. Again the powder was ground using the mortar and pestle. The final sample was prepared by passing the powder through the 2000 lpi mesh four times at decreasing power setting, the last being at 40 percent of full power. Great care was taken to ensure there was no contamination of the sub 5 μ m powder by larger particles or foreign materials.

3. Annealing

To avoid diffraction peak broadening or shifts due to induced stress created during the powdering process, the sample was annealed. The powder was put in a silica tube, placed under a vacuum of 1.5×10^{-6} torr, backfilled with helium, and sealed to prevent possible atmospheric contamination and to minimize aluminum loss due to alumina formation. The sample was then annealed at 900°C for one hour and furnace cooled to room temperature.

4. Powder Particle Size Measurement

Initial attempts to measure powder particle size were hampered by the inability to separately measure individual particles with the scanning electron microscope (SEM). The problem was solved by placing the powder back in the acoustic sieve assembly and passing a SEM sample holder coated with conductive paste under the sieve at 40 percent power; this method produced single, well separated particles and SEM particle size measurements were conducted at 2000X.

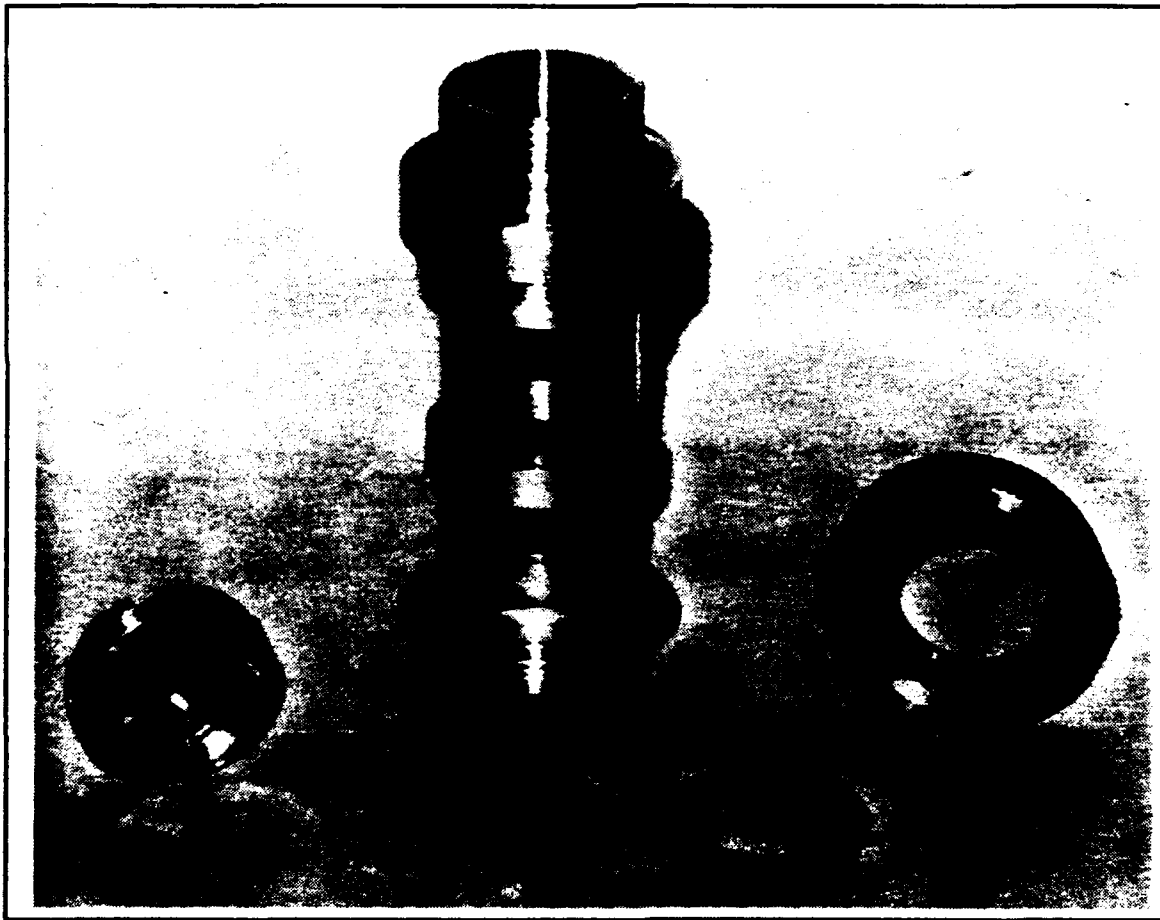


Figure 12. Sieve Assembly

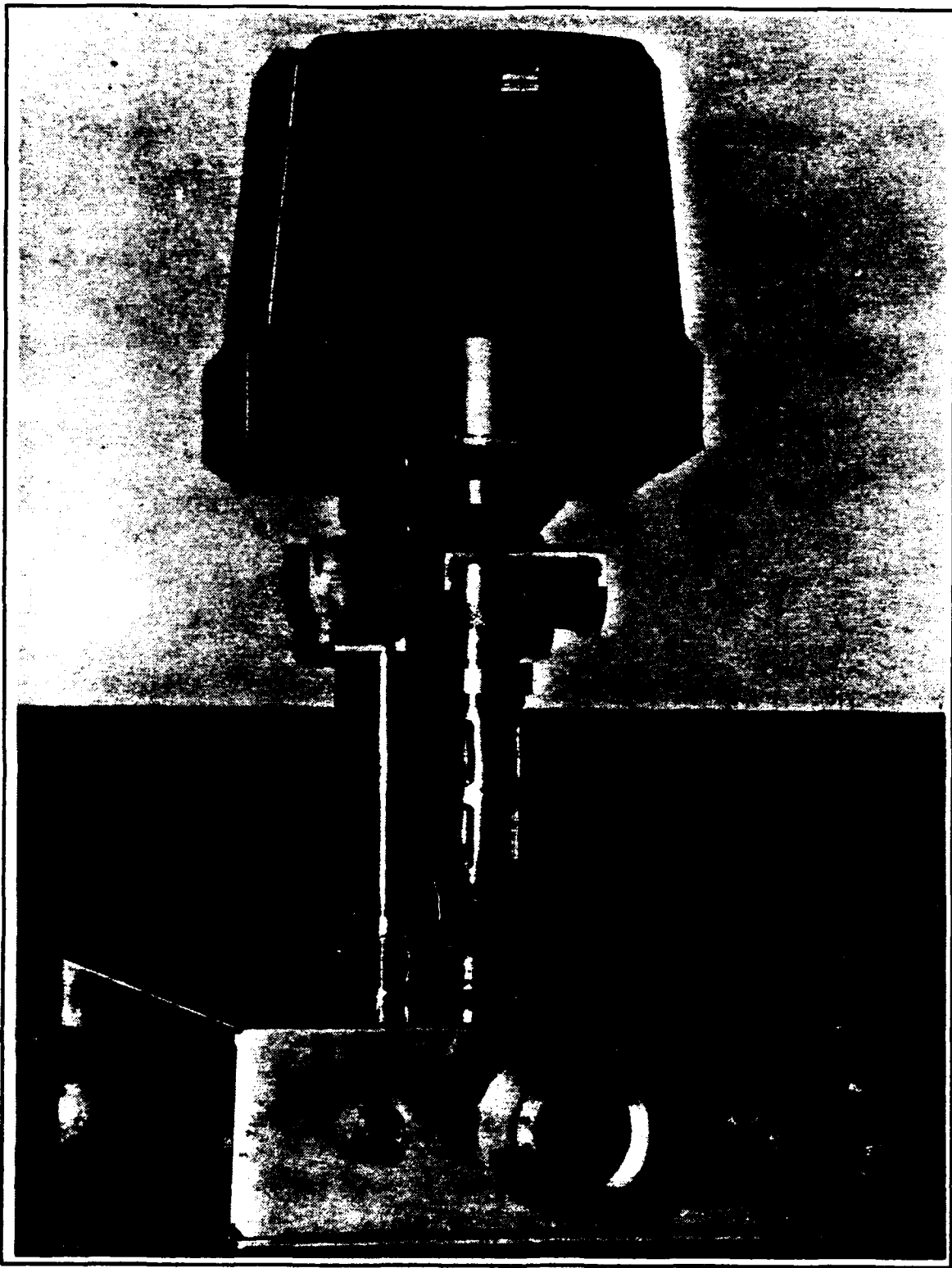


Figure 13. Acoustic Sieve

C. X-RAY DIFFRACTION

The annealed powder was mounted in the specimen holder with acetone using a modification of the procedure developed by McCreery and recommended by Klug and Alexander [Ref. 37: pp. 372-373].

The x-ray diffraction was performed using a Phillips XRG 3100 x-ray generator with a copper target and a power setting of 30kV and 35mA. A step size of 0.02 degrees with a 10 second scan time was used for the goniometer scan; this provided the scintillation type detector and attached Norelco Data Control and Processor with an accuracy of ± 0.005 degrees. Calibration using a quartz standard prior to XRD of the specimen indicated zero error between experimental and known peak positions.

The raw data was plotted using a VAX 3100 workstation and the peak positions and integrated intensities were determined and recorded using Phillips APD1700 software which curve fits each individual peak. The software calculations of integrated intensities were verified by carefully cutting out and weighing the raw data peaks from strip chart paper.

IV. RESULTS AND DISCUSSION

A. SAMPLE ANALYSIS

1. Previous Research

Wright-Patterson Air Force Base Materials Research Laboratory conducted an analysis of the specimen prior to heat treatment and that indicated an oxygen content of 700ppm by weight.

Cade's research indicated no presence of second phase or inclusions using optical microscopy. His inclusion study using SEM in conjunction with a Kevex Spectra Analyzer identified six fields out of 100 which contained any impurities. All six inclusions were $\leq 3\mu\text{m}$ in size and were deemed insignificant [Ref. 3: p. 38].

2. Powder Particle Size

Prior to annealing the specimen's particle size was investigated using a SEM at magnifications of 2000 and 4570. A sample of the observed particles are shown in Figure 14. The average particle size was on the order of $6\mu\text{m}$ and appeared to be disc like. Great care was taken to avoid the presence of any particles in excess of $10\mu\text{m}$. The largest particle viewed was elongated and approximately $8\mu\text{m}$ in length and $5\mu\text{m}$ in width. These type particles were believed to have passed

through the 2000 lpi sieve lengthwise. The average particle size was significantly less than Cade's $24.3 \pm 12.2 \mu\text{m}$ [Ref. 3: p. 47].



Figure 14. SEM Micrograph of Powder Particle Size at 2000X

B. X-RAY DIFFRACTION RESULTS

All measured diffraction peak positions and intensities are listed in Appendix A. The positions listed are the $\text{CuK}\alpha$ peaks (weighted average) produced using Phillips APD 1700 software. To verify the accuracy of the integrated intensities calculated using the software, each peak plot of raw data was carefully cut and weighed using a microbalance capable of measuring $\pm 0.1\text{mg}$. The (111) reflection was used to calibrate the calculated and weighed intensities and each peak was individually compared. The cross check showed very good correlation between the two methods of determining integrated intensities. The integrated intensities were then used to in conjunction with the calculated structure factors to determine the Debye-Waller factor by the Wilson Method.

The specimen's (111) diffraction peak is clearly seen shown in Figure 15. McCullough et al. produced the high temperature XRD profiles shown in Figure 16 [Ref. 12: p. 1325]. As can be seen through comparison of the two figures, the relatively small peaks on both sides of the experimental (111) peak are indications of the presence of an α -phase in addition to the known γ -phase of the specimen tested. The α -phase was probably formed during the heat treatment of the specimen as a result of the notable oxygen content.

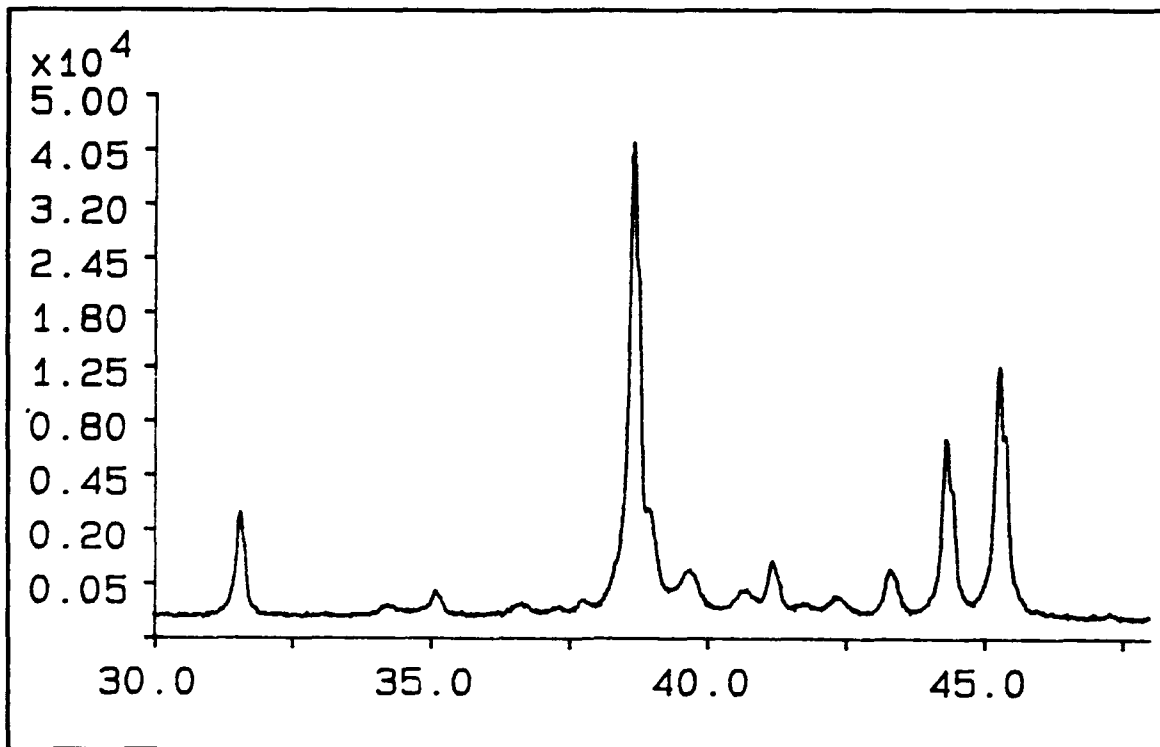


Figure 15. Specimen Tested Profile of (111) Diffraction Peak

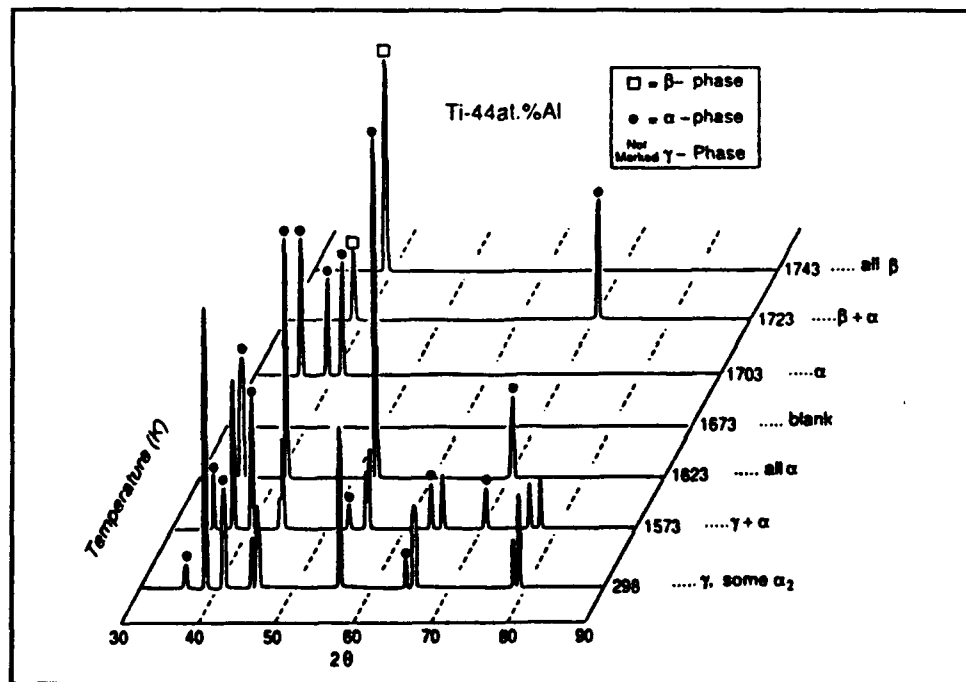


Figure 16. McCullough et al. High Temperature XRD TiAl Profiles

1. Lattice Parameters

The calculated lattice parameters and Nelson-Riley function values are tabulated in Appendix B. The extrapolation by least squares fit for lattice parameter a_0 is shown below; a_0 was determined to be 4.002\AA with a linear correlation of 0.98 for the seven peak positions plotted in Figure 17.

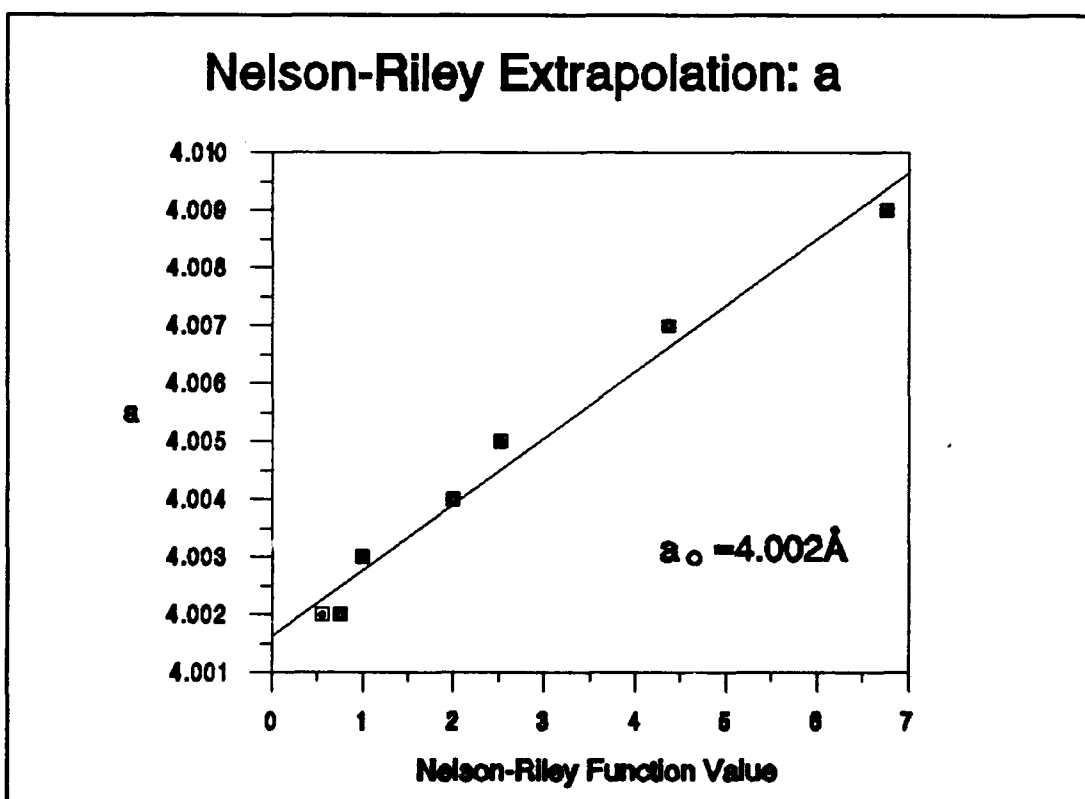


Figure 17. Nelson-Riley Extrapolation for Lattice Parameter a_0 .

Lattice parameter c_0 was determined to be 4.081\AA with a linear correlation of 0.73. The accuracy of c_0 is lower due to the reduced number of peak positions plotted in Figure 18.

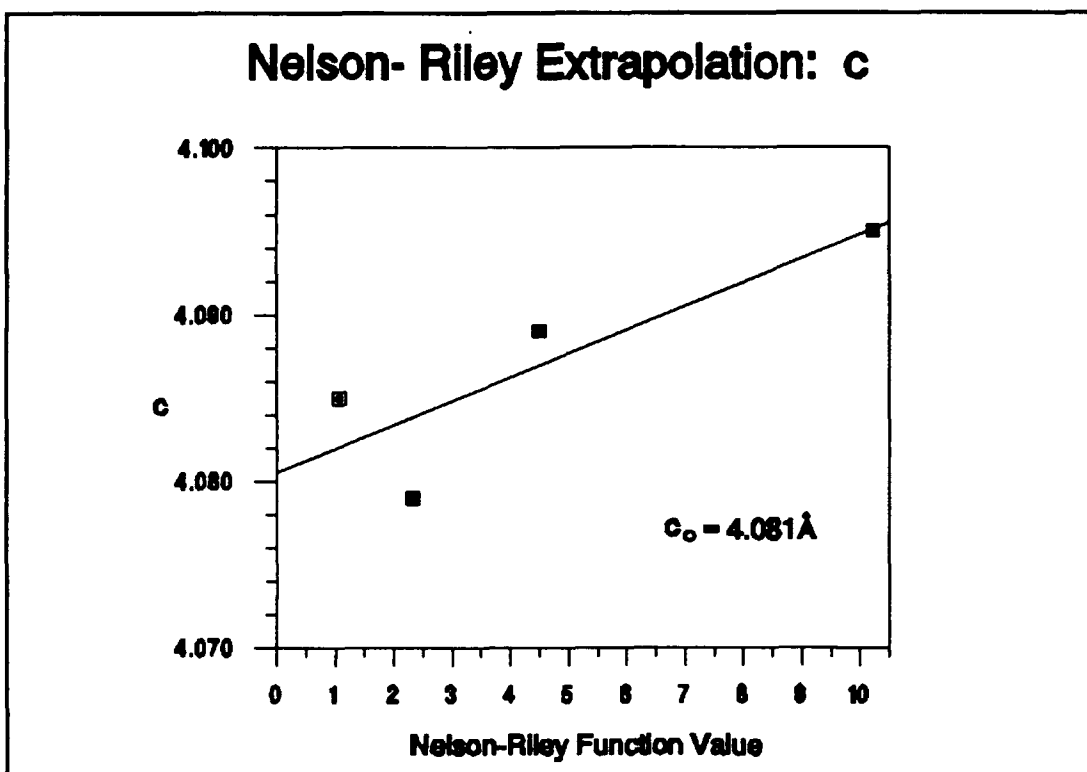


Figure 18. Nelson-Riley Extrapolation of Lattice Parameter c_0 .

The calculated values for a_0 and c_0 are slightly higher than those of Duwez and Taylor [Ref. 22: p.71] and Cade [Ref. 3: p. 40] however, the c/a ration of 1.02 agree quite favorably as shown in Figure 19 (plotted in kx units). Cade proposed the higher values were caused by overall increase in lattice parameter due to decreased number of vacancies formed by furnace cooling versus quenching after heat treatment. In numerous tests on near stoichiometric compositions, Valencia et al. have produced similar values to those obtained in this work [Ref. 19: p.1341].

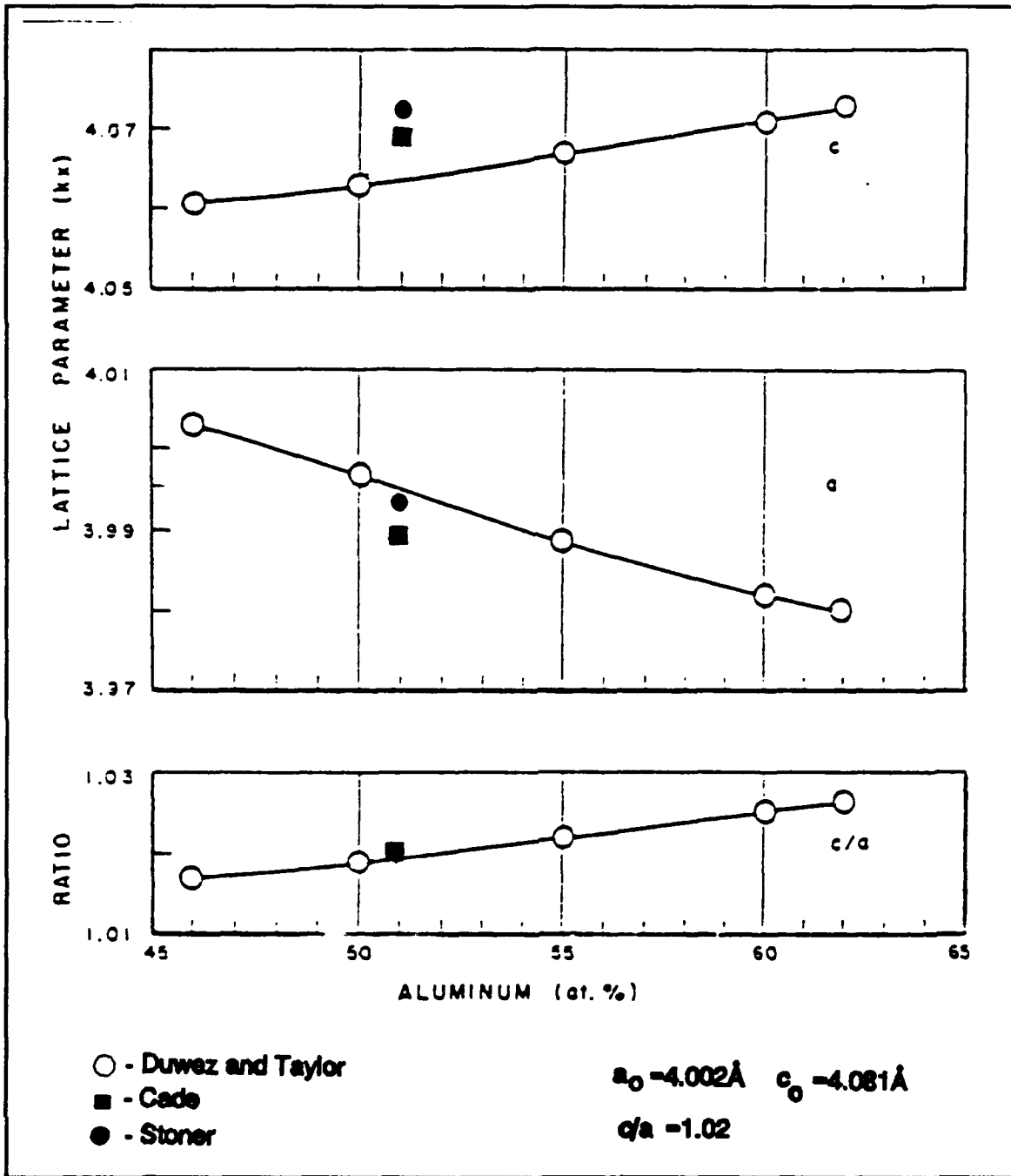


Figure 19. Lattice Parameter Comparison

2. Debye-Waller Factor

The Wilson plot data used for determining the Debye-Waller factors is tabulated in Appendix C. As in Cade's study, the values for the atomic structure factor were calculated using an analytical fit of scattering factor (f_o) data from Volume IV of the *International Tables* and the following equation [Ref. 3: p. 43] [Ref. 39: p. 71]:

$$f_o\left(\frac{\sin\theta}{\lambda}\right) = \sum_{i=1}^4 a_i \exp\left(-b_i \frac{\sin^2\theta}{\lambda^2}\right) + c \quad (25)$$

where a_i , b_i , and c are the coefficients for titanium and aluminum given in the *International Tables* [Ref. 39: p. 99]. For each reflection peak the dispersion correction factors ($\Delta f'$, $\Delta f''$) for Cu $K\alpha$ radiation from the *International Tables* were applied to f_o as per Equation 8 [Ref. 39: p. 149] [Ref. 42: p.214]. The corrected atomic structure factor (f) was then used to calculate the fundamental and superlattice structure factors using Equations 6 and 7 respectively.

The linear least squares fit for the fundamental reflections (004) and higher is shown in Figure 20. Low angle Bragg reflections were not included to avoid the effects of extinction observed below $(\sin^2\theta/\lambda^2)=0.5$, thus the Debye-Waller factor was determined to be $B=0.65\text{\AA}^2$ with a 0.86 linear correlation of the data.

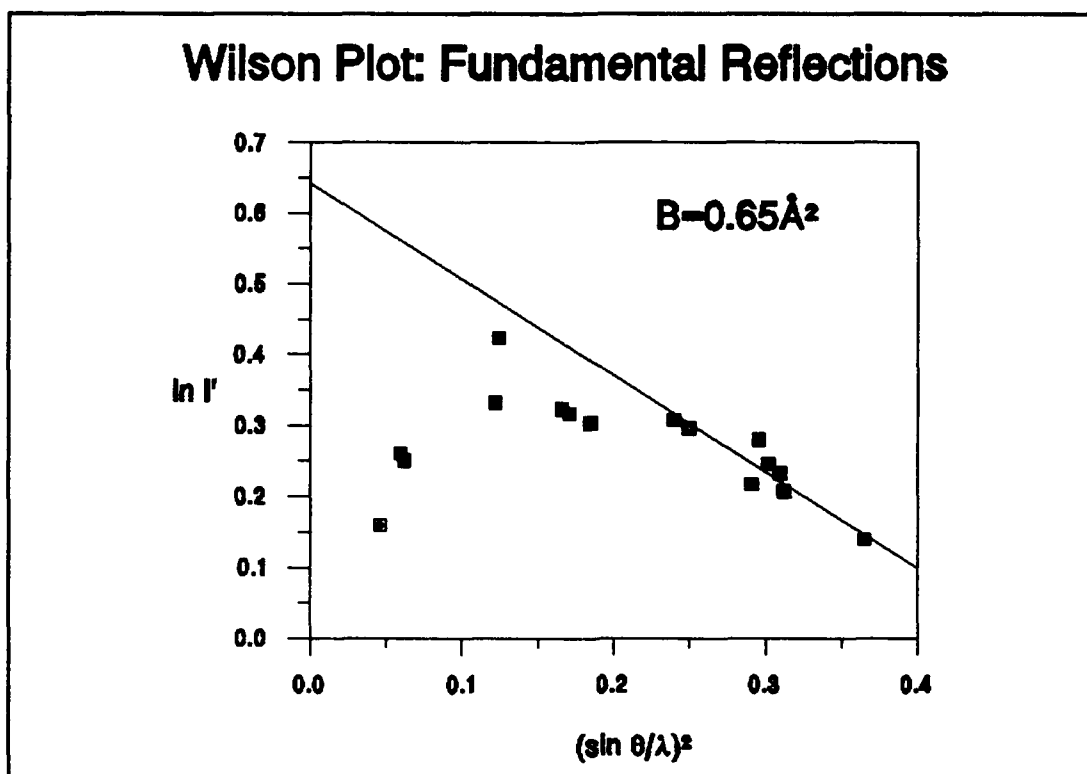


Figure 20. Debye-Waller Factor Determination from Fundamental Reflections

A theoretical approximation of the Debye-Waller factor TiAl was obtained using Equations 11 and 12. An average Debye temperature of $\Theta_D = 359 \text{ }^\circ\text{K}$ was calculated and the theoretical Debye-Waller factor was determined to be $B_{\text{THEORY}} = 0.74 \text{\AA}^2$. This is a very large approximation in that the equations used were derived for cubic and cubic monatomic elements respectively; the atomic r.m.s. amplitude constant was assumed to be 0.2; and the average of Ti and Al atomic weight was used. The Debye-Waller factors for the pure elements are $B_{\text{Ti}} = 0.55 \text{\AA}^2$ and $B_{\text{Al}} = 0.85 \text{\AA}^2$. Upon comparison of the experimentally determined $B = 0.65 \text{\AA}^2$ with

the theoretical approximation and Cade's measured $B=0.58\text{\AA}^2$, the data appears to be accurate.

The effects of extinction are clearly evident in Figure 21, but to see the significant improvement associated with powder particle size refinement a comparison plot was made using Cade's data and that from Appendix C. Cade's data was scaled using the difference in the Wilson plot intercepts. The comparison is shown in Figure 21 with the linear representation of $B=0.65\text{\AA}^2$ [Ref. 3: p. 44].

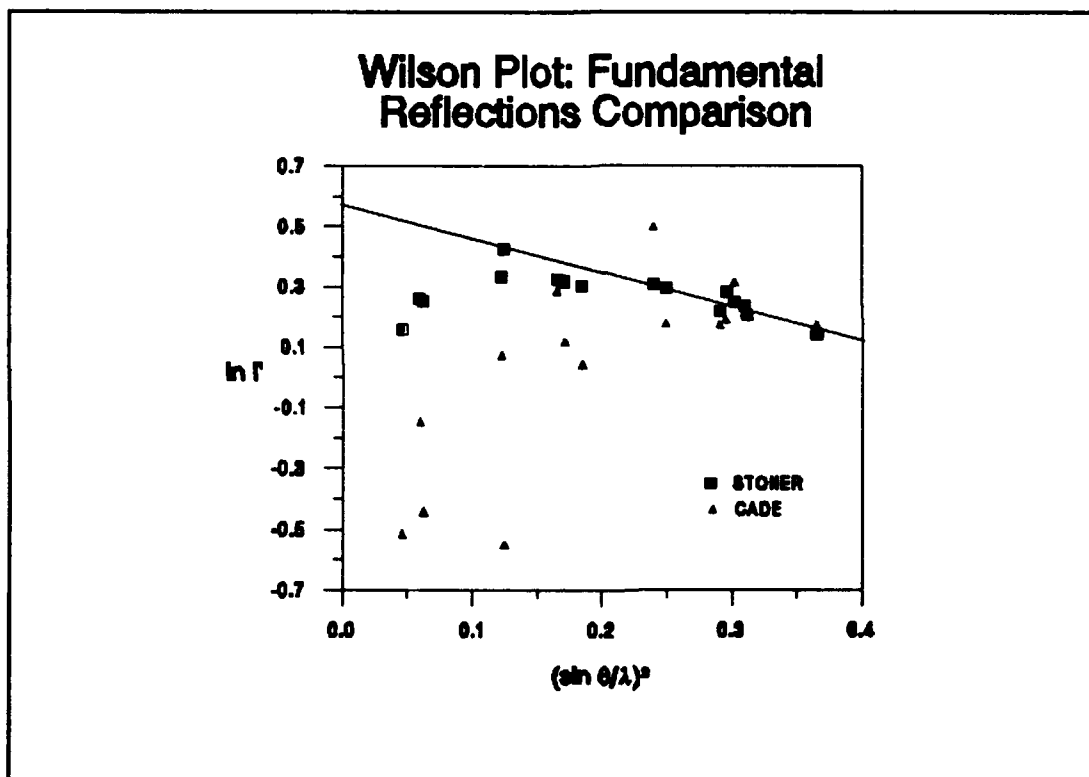


Figure 21. Extinction Effects Comparison from Fundamental Reflections

The Debye-Waller factor determination from superlattice reflections is shown in Figure 21. Again only the higher reflections were fitted and the resulting $B = 1.37\text{\AA}^2$ was determined with a 0.16 linear correlation. The low linear correlation (high deviation) is due to the relatively low intensities of superlattice reflections being more susceptible to measurement error. Subsequently the Debye-Waller factor determined from superlattice reflections was considered inaccurate. Note the linear representation in Figure 22 is for $B = 0.58\text{\AA}^2$, not $B = 1.37\text{\AA}^2$.

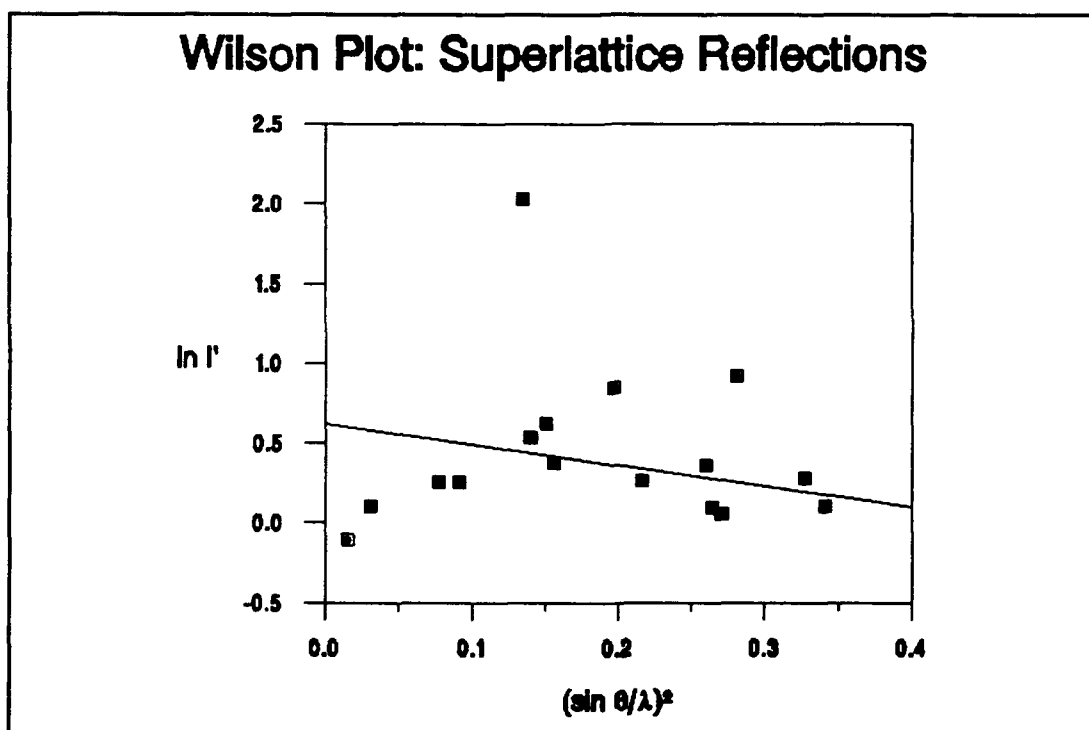


Figure 22. Debye-Waller Determination from Superlattice Reflections

The low angle extinction is reduced with the decrease in powder particle size yet remains readily apparent in both the fundamental and superlattice reflections.

V. CONCLUSIONS

Using powder X-ray diffraction procedures on an ostensibly extinction free γ Ti-51at.%Al alloy powder, this study's goals were: one, comparison and analysis of the improvements associated with refined powder particle size and two, the verification of previously measured lattice parameters and Debye-Waller temperature factors.

A new acoustic sieving method was used to produce an average powder particle size of $6\mu\text{m}$ in an attempt to alleviate low angle extinction effects. The two-fold reduction in size from Cade's previous study produced significant improvements in the measured intensities at low angles however, extinction effects for values of $(\sin^2\theta/\lambda^2) \leq 0.20$ were still large enough to prevent these low angle intensities from being included in Debye-Waller factor calculations.

The lattice parameters of the $L1_0$ structured TiAl were determined using an extrapolation of the Nelson-Riley function based on diffraction peak positions. The measured parameters were $a_0 = 4.002\text{\AA}$ and $c_0 = 4.081\text{\AA}$. These values were used to calculate an experimental c/a ratio of 1.02 for the tetragonal lattice of TiAl. The results closely matched that of previous research.

The Debye-Waller temperature factor of $B = 0.65\text{\AA}^2$ was determined from fundamental lattice reflections. This value compared very favorably with a

theoretical approximation based on characteristic temperatures and melting point data of titanium and aluminum, as well as, Cade's experimentally determined value. The Debye-Waller temperature factor from superlattice reflections was deemed inaccurate based on the high deviation due to the measurement error associated with the relatively low intensities of superlattice reflections.

Overall, the study produced very accurate results however, the effects of extinction were not completely remedied. Additional refinement in powder particle size and improved procedures for powder X-ray diffraction are required to further minimize the effects of low angle extinction in binary TiAl intermetallic alloy powders.

VI. RECOMMENDATIONS

The following recommendations are given for further study of TiAl intermetallic alloys and the determination of bonding characteristics using X-ray diffraction methods:

- Implement the acoustical sieve using >2000 lpi meshes to produce powder particle size averages below 5 μ m to avoid extinction effects.
- To minimize measured intensity deviation, a rotating specimen holder should be used to conduct multiple XRD scans, remounting the specimen after each scan. Then the average measured intensities should be used for Debye-Waller temperature factor calculations.
- Reduce the measurement error of the superlattice reflections by using smaller goniometer scan step sizes with longer scan times.
- Verify the accuracy of this study's results using critical voltage electron diffraction methods.
- Mathematically model the electron charge density of Ti-51at.%Al using the results of this study.
- Improve ingot metallurgical methods to reduce the amount of oxygen present and avoid formation of α -phase during heat treatment.
- Conduct further research to firmly establish the high temperature phase boundaries in the 30-60at.%Al range.

APPENDIX A. XRD REFLECTIONS AND INTEGRATED INTENSITIES

TABLE III. REFLECTION POSITIONS AND INTEGRATED INTENSITIES

Reflection (hkl)	Peak Position (degrees 2θ)	Experimental Intensity (counts)
001	21.69	24360
110	31.55	21710
111	38.65	361900
002	44.29	66370
200	45.25	122800
201	50.76	11720
112	55.44	8470
202	65.23	82470
220	65.97	43440
003	69.07	5610
221	70.38	4715
103	73.60	4440
130	75.01	3520
113	77.81	47210
131	79.20	89130
222	82.99	38840

TABLE III. (Continued)

Reflection (hkl)	Peak Position (degrees 2θ)	Experimental Intensity (counts)
203	86.44	3570
132	91.52	3590
004	98.03	7090
400	100.77	13610
223	103.57	1800
401	104.96	1370
114	106.74	1340
330	109.62	1600
313	112.53	48620
331	114.00	25990
204	115.90	25370
402	118.18	25520
420	118.95	25160
421	123.74	4040
332	128.39	1880
224	137.26	30860

APPENDIX B. NELSON-RILEY EXTRAPOLATION DATA

TABLE IV. NELSON-RILEY EXTRAPOLATION DATA (a)

Reflection (hkl)	θ (degrees)	Value of Nelson-Riley Function	a (Å)
100	15.78	6.770	4.009
200	22.63	4.372	4.007
220	32.99	2.515	4.005
130	37.51	1.995	4.004
400	50.39	0.9901	4.003
330	54.81	0.7535	4.002
420	59.48	0.5480	4.002

TABLE V. NELSON-RILEY EXTRAPOLATION DATA (c)

Reflection (hkl)	θ (degrees)	Value of Nelson-Riley Function	c (Å)
001	10.85	10.22	4.095
002	22.15	4.496	4.089
003	34.54	2.323	4.079
004	49.02	1.073	4.085

APPENDIX C. WILSON PLOT DATA

TABLE VI. WILSON PLOT DATA: FUNDAMENTAL REFLECTIONS

Reflection (hkl)	$(\sin\theta/\gamma)^2$ (\AA^{-2})	$p\phi(\theta)F^2$ (counts)	I_{exp} (counts)	$\ln I'$ *
111	0.0461	308400	361900	0.1600
002	0.0598	51120	66370	0.2611
200	0.0623	95530	122800	0.2511
202	0.1222	59140	82470	0.3325
220	0.1247	28430	43440	0.4238
113	0.1659	34160	47210	0.3234
131	0.1709	64900	89130	0.3172
222	0.1847	28670	38840	0.3032
004	0.2397	5206	7090	0.3080
400	0.2496	10120	13610	0.2960
313	0.2909	39080	48620	0.2179
331	0.2959	19650	25990	0.2796
204	0.3022	19820	25370	0.2469
402	0.3097	20200	25520	0.2331
420	0.3122	20450	25160	0.2073
224	0.3648	26830	30860	0.1400

* $\ln I' = \ln(I_{\text{exp}}/p\phi(\theta)F^2)$ as per the Wilson Method.

TABLE VII. WILSON PLOT DATA: SUPERLATTICE REFLECTIONS

Reflection (hkl)	$(\sin\theta/\gamma)^2$ (\AA^{-2})	$p\phi(\theta)F^2$ (counts)	I_{exp} (counts)	$\ln I^*$
001	0.0149	27020	24360	-0.1041
110	0.0311	19570	21710	0.1036
201	0.0773	9040	11720	0.2590
112	0.0910	6560	8470	0.2543
003	0.1352	740	5610	2.0297
221	0.1397	2750	4715	0.5387
103	0.1510	2370	4440	0.6265
130	0.1559	2230	3250	0.3761
203	0.1973	1520	3570	0.8526
132	0.2159	2740	3590	0.2651
223	0.2597	1240	1800	0.3651
401	0.2646	1240	1370	0.0961
114	0.2709	1250	1340	0.0554
330	0.2810	630	1600	0.9206
421	0.3272	3040	4040	0.2830
332	0.3410	1670	1880	0.1022

* $\ln I^* = \ln(I_{\text{exp}}/p\phi(\theta)F^2)$ as per the Wilson Method.

LIST OF REFERENCES

1. Khataee, A., Flower, H. M., and West, D. R., "New Titanium-Aluminum-X Alloys for Aerospace Applications," *Journal of Materials Engineering* Vol. 10, No. 1, pp. 37-44, 1988.
2. Khataee, A., Flower, H. M., and West, D. R. F., "The alloying of Titanium Aluminides with Ruthenium," *Platinum Metals Review*, Vol. 33, No. 3, pp.106-113, 1989.
3. Cade, Steven C., *An Investigation of the Interatomic Bonding Characteristics of a γ Ti-51at% Al Alloy by X-Ray Diffraction*, MS Thesis, Naval Postgraduate School, 1991.
4. Lipsitt, H. A., "Titanium Aluminides--An Overview," *Materials Research Society Symposium Proceedings*, Vol. 39, pp. 351-364, 1986.
5. Konitzer, D.G., Jones, I.P., and Fraser, H.L. "Site Occupancy in Solid Solutions of Nb in the Intermetallic Compounds TiAl and Ti₃Al," *Scripta Metallurgica*, Vol. 20, No. 2, pp. 265-268, 1986.
6. Sundaresan, R., and Froes, F.H., "Titanium Intermetallics Development Through Mechanical Alloying," *Metal Powder Report*, Vol. 44, No. 3, pp. 206-208, 1989.
7. Benn, R.C., Mirchandani, P.K., and Watwe, A.S., "Intermetallic Systems Produced by Mechanical Alloying," *Proceedings of the 1988 International Powder Metallurgy Conference*, Vol. 21, pp. 479-493, American Powder Metallurgy Institute, 1988.
8. Yamaguchi, M., and Umakoshi, Y., "The Deformation Behaviour of Intermetallic Superlattice Compounds," *Progress in Materials Science*, Vol. 34, pp. 1-148, 1990.
9. Court, S.A., Vasudevan, V.K., and Fraser, H.L., "Deformation Mechanisms in the Intermetallic Compound TiAl," *Philosophical Magazine A*, Vol. 61, No. 1, pp. 141-158, 1990.

10. Woodward, C., MacLaren, J.M., and Rao, S., "Electronic Structure of Planar Faults in TiAl," Submitted for publication in *Journal of Materials Research*, 1991.
11. MacClaren, J.M. and Woodward, C., "Electronic Structure of Planar Faults and Point Defects in High Temperature Intermetallics," Submitted for presentation at the *Materials Research Society*, Fall 1991.
12. McCullough, C., Valencia, J.J., Levi, C.G., and Mehrabian, R., "Phase Equilibria and Solidification in Ti-Al Alloys," *Acta Metallurgica*, Vol. 37, No. 5, pp. 1321-1336, 1989.
13. Sircar, Subhasish, *Phase Transitions in High Temperature Ordered Intermetallic Titanium Aluminum Alloys*, Ph.D. Dissertation, Michigan State University, 1987.
14. Graves, J.A., and Ghosh, A.K., "Microstructure and Elevated Temperature Flow Properties of Rapidly Solidified TiAl-Base Alloys," *Proceedings of the Third Symposium on High-Temperature Ordered Intermetallic Alloys*, pp. 317-322, Materials Research Society, 1989.
15. Ogden, H.R., Maykuth, D.J., Finlay, W.L., and Jaffee, R.I., "Constitution of Titanium-Aluminum Alloys," *Transactions AIME*, Vol 191, pp. 1150-1155, 1951.
16. Murray, J.L., in *Binary Alloy Phase Diagrams*, Vol. 1, pp. 225-227, ASM International, 1990.
17. Shull, R.D., McAlister, A.J., and Reno, R.C., "Phase Equilibria in the Titanium-Aluminum System," *Proceedings of the Fifth International Conference on Titanium*, Vol. 3, pp. 1459-1466, 1985.
18. Murray, J.L., "Calculations of the Titanium-Aluminum Phase Diagram," *Metallurgical Transactions A*, Vol. 19A, pp. 243-247, 1988.
19. Valencia, J.J., McCullough, C., Levi, C.G., and Mehrabian, R., "Microstructure Evolution During Conventional and Rapid Solidification of Ti-50at.%Al Alloy," *Scripta Metallurgica*, Vol. 21, No. 10, pp. 1341-1346, 1987.
20. McCullough, C., Valencia, J.J., Mateos, H., Levi, C.G., and Mehrabian, R., "The High Temperature α Field in the Titanium-Aluminum Phase Diagram," *Scripta Metallurgica*, Vol. 21, No. 10, pp. 1131-1136, 1988.

21. Willey, I.A., and Margolin, H., in *Metals Handbook*, 8th ed., Vol. 8, ASM, Metals Park, OH, 1973, p. 264.
22. Duwez, P., and Taylor, J.L., "The Crystal Structure of TiAl," *Transactions AIME*, Vol. 194, pp. 70-71, 1952.
23. Li, Z.X., Li, Z.C., and Whang, S.H., "Long-Range Ordering in Rapidly Quenched Ti-Al Compounds", *Materials Science and Engineering*, Vol. 98, pp. 169-172, 1988.
24. Schechtman, D., Blackburn, M.J., and Lipsitt, H.A., "The Plastic Deformation of TiAl," *Metallurgical Transactions*, Vol. 5, No. 6, pp. 1373-1381, 1974.
25. Lipsitt, H.A., Shechtman, D., and Schatrik, R.E., "The Deformation and Fracture of TiAl at Elevated Temperatures," *Metallurgical Transactions*, Vol. 6A, pp. 1991-1996, 1975.
26. Huang, S.C., and Hall, E.L., "Plastic Deformation and Fracture of Binary TiAl-Base Alloys," *Metallurgical Transactions A*, Vol. 22A, No. 2, pp. 427-438, 1991.
27. Hug, G., Loiseau, A., and Lasalmonie, A., "Nature and Dissociation of the Dislocations in TiAl Deformed at Room Temperature," *Philosophical Magazine A*, Vol. 54, No. 1, pp. 47-65, 1986.
28. Hug, G., Loiseau, A., and Veysière, P., "Weak Beam Observation of a Dissociation Transition in TiAl", *Philosophical Magazine*, Vol. 57, No. 3, pp. 499-523, 1988.
29. Greenberg, B.A., Anisimov, V.I., Gornostirev, Yu.N., and Taluts, G.G., "Possible Factors Affecting the Brittleness of the Intermetallic Compound TiAl," *Scripta Metallurgica*, Vol. 22, No. 6, pp. 859-864, 1988.
30. Feng, C.R., Michel, D.J., and Crowe, C.R., "Twinning Relationships in TiAl", *Scripta Metallurgica*, Vol. 22, pp. 1481-1486, 1988.
31. Feng, C.R., Michel, D.J., and Crowe, C.R., "Twinning in TiAl", *Scripta Metallurgica*, Vol. 23, pp. 1135-1140, 1989.
32. Fox, A.G., and Tabbernor, M.A., "The Bonding Charge Density of β NiAl", *Acta Metallurgica*, Vol. 39, No. 4, pp. 669-678, 1991.

33. Takama, T., and Sato, S., "Accurate determination of Structure Factors by Pendellösung Methods using White Radiation", *Australian Journal of Physics*, Vol. 41, pp. 433-448, 1988.
34. Fox, A.G., and Fisher, R.M., "A Summary of Low-angle X-ray Atomic Scattering Factors Measured by the Critical Voltage Effect in High Energy Electron Diffraction," *Australian Journal of Physics*, Vol. 41, pp. 461-468, 1991.
35. Cooper, M.J., "The Electron Distribution in the Phases of CoAl and NiAl," *Philosophical Magazine*, Vol. 8, pp. 811-821, 1963.
36. Hughes, T., Lautenschlager, E.P., Cohen, J.B., and Brittain, J.O., " X-Ray Diffraction Investigation of β' -NiAl Alloys," *Journal of Applied Physics*, Vol. 42, No. 10, pp. 3705-3716, 1971.
37. Klug, H.P., and Alexander, L.E., *X-Ray Diffraction Procedures*, 2nd ed., John Wiley & Sons, 1974.
38. Cullity, B.D., *Elements of X-Ray Diffraction*, 2nd ed., Addison-Wesley, 1978.
39. *International Tables for X-Ray Crystallography*, Vol. IV, pp. 45-151, The Kynoch Press, 1974.
40. Ziman, J.M., *Principles of the Theory of Solids*, p. 63, Cambridge University Press, 1969.
41. *International Tables for X-Ray Crystallography*, Vol. II, pp. 242-265, The Kynoch Press, 1959.
42. *International Tables for X-Ray Crystallography*, Vol. III, pp. 232-244, The Kynoch Press, 1962.
43. Willis, B.T.M., and Pryor, A.W., *Thermal Vibrations in Crystallography*, Cambridge University Press, Ch. 4, 1975.

INITIAL DISTRIBUTION LIST

	No. Copies
1. Defense Technical Information Center Cameron Station Alexandria, Virginia 22304-6145	2
2. Library, Code 52 Naval Postgraduate School Monterey, California 93943-5002	2
3. Department Chairman, Code ME/Hy Department of Mechanical Engineering Naval Postgraduate School Monterey, California 93943-5000	1
4. Weapons Engineering Curricular Office, Code 33 Naval Postgraduate School Monterey, California 93943-5000	1
5. Dr. Jeff Waldman Code 6063 Naval Air Development Center Warminster, Pennsylvania 18974	1
6. Dr. Alan G. Fox, Code ME/Fx Department of Mechanical Engineering Naval Postgraduate School Monterey, California 93943-5000	2
7. LT Troy A. Stoner, USN RT 2 Grange Hall RD Hanover, Indiana 47243	2